Engineered Extracellular Vesicles Derived from Dermal Fibroblasts Attenuate Inflammation in a Murine Model of Acute Lung Injury

Ana I. Salazar-Puerta, María A. Rincon-Benavides, Tatiana Z. Cuellar-Gaviria, Julian Aldana, Gabriela Vasquez Martinez, Lilibeth Ortega-Pineda, Devleena Das, Daniel Dodd, Charles A. Spencer, Binbin Deng, David W. McComb, Joshua A. Englert, Samir Ghadiali, Diana Zepeda-Orozco, Loren E. Wold, Daniel Gallego-Perez, and Natalia Higuita-Castro*

Acute respiratory distress syndrome (ARDS) represents a significant burden to the healthcare system, with ≈200 000 cases diagnosed annually in the USA. ARDS patients suffer from severe refractory hypoxemia, alveolar-capillary barrier dysfunction, impaired surfactant function, and abnormal upregulation of inflammatory pathways that lead to intensive care unit admission, prolonged hospitalization, and increased disability-adjusted life years. Currently, there is no cure or FDA-approved therapy for ARDS. This work describes the implementation of engineered extracellular vesicle (eEV)-based nanocarriers for targeted nonviral delivery of anti-inflammatory payloads to the inflamed/injured lung. The results show the ability of surfactant protein A (SPA)-functionalized *IL-4-* and *IL-10*-loaded eEVs to promote intrapulmonary retention and reduce inflammation, both in vitro and in vivo. Significant attenuation is observed in tissue damage, proinflammatory cytokine secretion, macrophage activation, influx of protein-rich fluid, and neutrophil infiltration into the alveolar space as early as 6 h post-eEVs treatment. Additionally, metabolomics analyses show that eEV treatment causes significant changes in the metabolic profile of inflamed lungs, driving the secretion of key anti-inflammatory metabolites. Altogether, these results establish the potential of eEVs derived from dermal fibroblasts to reduce inflammation, tissue damage, and the prevalence/progression of injury during ARDS via nonviral delivery of anti-inflammatory genes/transcripts.

1. Introduction

Acute respiratory distress syndrome (ARDS) represents a significant burden to health systems worldwide,[1–4] considering the need for critical care, prolonged hospitalization times, and slow recovery.[1] Pre-COVID-19 there were ≈200 000 cases of ARDS reported annually in the United States.[5–8] The mortality rate for patients with ARDS is high , ranging between 25% and 40%.[6] ARDS is the most severe form of acute lung injury and is normally caused by direct or indirect injury to the lung (i.e., infections, trauma, pneumonia, hemorrhagic shock, among others).[9–11] Once the lung is injured, there is significant upregulation of proinflammatory pathways, with marked recruitment of neutrophils, and significant secretion of proinflammatory cytokines and other mediators.[5,6] Although inflammation is critical for the resolution of the underlying condition, hyperinflammation can lead to capillary injury, and further disruption of the alveolar-capillary barrier, followed by a significant influx of protein-rich fluid

A. I. Salazar-Puerta, M. A. Rincon-Benavides, T. Z. Cuellar-Gaviria,
L. Ortega-Pineda, D. Das, D. Dodd, S. Ghadiali, D. Gallego-Perez,
N. Higuita-Castro
Department of Biomedical Engineering
The Ohio State University
Columbus, OH 43210, USA
E-mail: higuitacastro.1@osu.edu
M. A. Rincon-Benavides, D. Gallego-Perez, N. Higuita-Castro
Biophysics Program
The Ohio State University
Columbus, OH 43210, USA

**ADVANCED
SCIENCE NEWS**

www.advancedsciencenews.com

**ADVANCED
MATERIALS**

www.advmat.de

into the alveolar space.[12–14] This accumulation of edema fluid in the interstitium and alveolar space causes impaired gas exchange and results in poor oxygenation, reduced carbon dioxide excretion, decreased lung compliance, and ultimately acute respiratory failure. For patients with ARDS, mechanical ventilation is used as supportive therapy to maintain adequate oxygenation. However, the mechanical stress imposed during ventilation exacerbates the initial injury and triggers a positive feedback loop that favors inflammation, which could lead to multisystem organ dysfunction/failure and death.[7,10]

Currently, there is no cure or FDA-approved therapy for ARDS.[15] This unmet clinical need is especially important considering the recent COVID-19 pandemic, where 67% of COVID-19 patients have developed ARDS,[16–19] and in which

J. Aldana
Biochemistry Program
The Ohio State University
Columbus, OH 43210, USA

G. Vasquez Martinez, D. Zepeda-Orozco
Kidney and Urinary Tract Research Center
The Abigail Wexner Research Institute
Nationwide Children's Hospital
Columbus, OH 43215, USA

D. Dodd
Biomedical Science Graduate Program
The Ohio State University
Columbus, OH 43210, USA

C. A. Spencer, L. E. Wold
Division of Cardiac Surgery
Department of Surgery
The Ohio State University
Columbus, OH 43210, USA

B. Deng, D. W. McComb
Center for Electron Microscopy and Analysis (CEMAS)
The Ohio State University
Columbus, OH 43212, USA

D. W. McComb
Department of Materials Science and Engineering
The Ohio State University
Columbus, OH 43210, USA

J. A. Englert, S. Ghadiali
Division of Pulmonary, Critical Care, and Sleep Medicine
The Ohio State University
Columbus, OH 43221, USA

D. Zepeda-Orozco
Department of Pediatrics
The Ohio State University
Columbus, OH 43210, USA

D. Zepeda-Orozco
Division of Pediatric Nephrology and Hypertension
Nationwide Children's Hospital
Columbus, OH 43205, USA

D. Gallego-Perez, N. Higuita-Castro
Division of General Surgery
Department of Surgery
The Ohio State University
Columbus, OH 43210, USA

D. Gallego-Perez, N. Higuita-Castro
Dorothy M. Davis Heart & Lung Research Institute
The Ohio State University
Columbus, OH 43210, USA

D. Gallego-Perez, N. Higuita-Castro
Gene Therapy Institute
The Ohio State University
Columbus, OH 43210, USA

lung inflammation has played a critical role in determining clinical outcomes. Although progenitor cell-based therapies (e.g., endothelial progenitor cells, and mesenchymal stem cells) have been explored to reduce inflammation and enhance lung repair via trophic and anti-inflammatory mechanisms (e.g., through the secretion of multiple effector molecules, including anti-inflammatory cytokines, growth factors, and antimicrobial peptides),[7,8,13,20–23] significant concerns remain with respect to potential tumorigenesis, high immunogenic responses, limited cell sources, cumbersome and labor-intensive ex vivo processing, and effective delivery methods.[24,25] On the other hand, while the use of anti-inflammatory approaches to treat the pathophysiology of ARDS has shown significant promise, efficient delivery to the inflamed lung environment remains a major challenge in critically ill patients.[26–28]

Extracellular vesicles (EVs) are cell-derived natural carriers that play a crucial role in mediating short- and long-range cell-cell communication, and share molecular cues with their donor cell.[29–32] EVs have been known to exhibit high stability in biofluids, low immunogenicity, and exceptional biocompatibility. Furthermore, EVs possess an innate ability to cross biological barriers, to transport and deliver a variety of active biomolecules, including proteins, antigens, and nucleic acids, among others, without significant restrictions on size.[33–35] Even though EVs still face some limitations (e.g., heterogeneity,[36,37] paucity of standardized isolation and purification protocols,[37,38] and large-scale production for clinical use),[39,40] they have emerged as promising drug- and gene-delivery nanocarriers capable of circumventing some of the practical and translational barriers faced by standard nanocarrier systems.[41,42]

We have previously shown that donor cells can be engineered to stimulate the release of engineered (eEVs) packed with specific molecular cargo for diverse therapeutic applications and that eEVs can be functionalized with ligands of interest to achieve targeted delivery to cells and tissues.[43–49] Here we report on the implementation of eEVs derived from dermal fibroblasts, loaded with genes, mRNA transcripts, and protein content of anti-inflammatory cytokines interleukin-4 and -10 (IL-4 and IL-10), to dampen lung injury and inflammation, and decorated with Surfactant Protein A (SPA) to promote preferential retention by cell compartments in the injured lung. SPA is an abundant glycoprotein component present in the lung surfactant, which is implicated in the reduction of the surface tension at the pulmonary air–liquid interphase, prevention of alveolar collapse, and is also considered a major inflammatory immunomodulator.[50,51] In light of this, in addition to enabling targeted delivery to the lung, the presence of mRNA transcripts of SPA in the eEVs could potentially boost the attenuation of lung inflammation due to its role in maintaining immune homeostasis in the lung microenvironment.[52]

These anti-inflammatory eEVs were derived 24 h after nonviral electrotransfection of adult mouse dermal fibroblasts. Our results highlight the ability of *IL-4-* and *IL-10*-loaded eEVs to reduce lipopolysaccharide (LPS)-induced lung inflammation and tissue damage, in vitro and in vivo. In vitro, we observed significant attenuation of proinflammatory cytokine secretion (IL-6, IL-1β, and TNF-α), and macrophage activation. In vivo, we also observed a significant reduction in the secretion of proinflammatory cytokines (IL-6, IL-1β, and TNF-α), protein-rich fluid influx

into the alveolar space, neutrophil infiltration, and tissue damage in mice treated with *IL-4-* and *IL-10*-loaded eEVs as early as 6 h after treatment. In vivo studies suggest that the decoration of eEVs with the SPA targeting ligand improves intrapulmonary eEV retention. Metabolomics analyses also demonstrated that anti-inflammatory eEVs also had a significant impact on the metabolic profile of LPS-challenged mice by inducing the secretion of metabolites related to key anti-inflammatory pathways. These results establish the potential of using anti-inflammatory eEVs, obtained via nonviral approaches, to reduce inflammation and the prevalence/progression of lung injury during ARDS.

2. Results

2.1. Electrotransfection of Dermal Fibroblasts with *IL-4*, *IL-10*, and *SPA* Leads to the Release of SPA-Decorated eEVs Loaded with *IL-4* and *IL-10*

eEVs were derived from adult-mouse dermal fibroblast (MDF) cultures electrotransfected with expression plasmids for anti-inflammatory cytokines *IL-4* or *IL-10* and the targeting ligand SPA (**Figure 1**A). EVs released from MDF cultures electrotransfected with a sham/empty pCMV6 vector were used as control (i.e., sham eEVs). Western blot analysis confirmed the presence of the EV marker CD63 and the cytoskeletal marker tubulin in the donor cells, *IL-10+SPA*, *IL-4+SPA*, and sham eEVs, and a reduced expression of the endoplasmic reticulum protein calnexin detected in eEV formulations compared to donor cells (Figure 1B). Additional EV marker proteins, including ALG-2-interacting protein X (ALIX) and tumor susceptibility gene 101 protein (TSG101) were also found in the eEV formulations and donor cells (Figure S1A, Supporting Information). Nanoparticle tracking analysis indicated that 24 h after transfection, adult MDFs release eEVs in the order of $5.7–6.11 \times 10^{10}$ eEVs mL^{-1}, with an average size ranging between 190 and 226 nm for sham and anti-inflammatory eEVs, respectively (Figure 1C, and Figure S1B, Supporting Information). Morphological characterization of the eEVs performed via Cryo-electron microscopy (Cryo-EM) revealed discrete eEVs with an intact structure and a characteristic lipid-bilayer (Figure 1D). qRT-PCR analyses confirmed successful transfection of adult-MDF, with significant overexpression of *IL-4* and *IL-10* after 24 h (Figure 1E). Adult-MDF also showed significant overexpression of the targeting ligand *SPA* for cells cotransfected with *IL-4+SPA* or *IL-10+SPA*, compared to sham-transfected cells (Figure 1F). We also observed that the cotransfection of *IL-10+SPA*, had a boosting effect on *IL-10* expression in the donor cells, with an increase of approximately two-fold compared to cells electrotransfected only with *IL-10* (Figure 1E,F) (*p*-value = 0.0140). qRT-PCR characterization of eEV content confirmed robust packing with transcripts for *IL-4* and *IL-10*, 24 h after electrotransfection of the donor cells with plasmids encoding for *IL-4, IL-10, IL-4+SPA*, or *IL-10+SPA* (Figure 1G,H). Additionally, we also verified that there is IL-4 and IL-10 protein content associated with the eEVs as confirmed via enzyme-linked immunosorbent assay (ELISA) of IL-4+SPA and IL-10+SPA eEV formulations, compared to sham eEVs (Figure 1I,J). Collectively, these results demonstrate the feasibility of packing transcripts of anti-inflammatory cytokines *IL-4* and *IL-10* in eEVs and function-

alizing them with the targeting ligand SPA on their membrane to improve intrapulmonary/alveolar interaction and retention.

2.2. Anti-Inflammatory eEVs Dampen LPS-Induced Inflammation In Vitro

Activated monocytes play a major role in the secretion of proinflammatory cytokines in response to the activation of pattern recognition receptors by pathogen- or damage-associated molecular patterns.[53,54] We optimized an in vitro inflammation model where RAW 264.7 macrophage cells were challenged with 100–1000 ng mL^{-1} LPS for 3–48 h to induce significant upregulation of key proinflammatory mediators such as IL-6, IL-1β, iNOS, and TNFα (Figure S2, Supporting Information). To evaluate the therapeutic potential of eEVs in dampening inflammation, macrophages challenged with 100 ng mL^{-1} LPS were co- or post-treated with *IL-4+SPA, IL-10+SPA*, or sham eEVs (**Figures 2**A and **3**A). Cell cultures that were not exposed to LPS (i.e., control) or LPS-challenged without any eEV treatment (i.e., LPS) were included for comparison purposes. For post-treatment experiments, cells that had been LPS-challenged for 12 h were exposed to eEVs at a concentration of $\approx$2000 eEVs/cell for 3–6 h. Subsequently, the inflammatory response was evaluated in terms of altered cell morphology, gene expression via qRT-PCR, and protein secretion via ELISA. Early changes in cell morphology were indicative and consistent with successful monocyte/macrophage activation in response to the LPS challenge, where activated cells presented a characteristic spindle shape with reduced roundness compared to unchallenged cells (Figure 2B). LPS- macrophages that were eEV-treated for 3 and 6 h with *IL-4+SPA* or *IL-10+SPA* eEVs showed a significant decrease in the number of activated monocytes compared to control groups (Figure 2B and Figure S3A, Supporting Information). We also observed a significant decrease in the expression levels of *IL-6* and *IL-1β* for cells post-treated with *IL4+SPA* eEVs for 3 and 6 h compared to controls (Figure 2C and Figure S3B, Supporting Information). On the other hand, cells treated with *IL-10+SPA* eEVs only showed a significant reduction in the expression levels of *IL-6* and *IL-1β* at 3 h post-treatment compared to controls (Figure 2C). Similarly, in terms of protein expression, *IL-4+SPA* eEV-treated cells showed a significant reduction in the secretion of IL-6, IL-1β, and TNFα at 3 h post-treatment compared to controls (Figure 2D), while cells treated with *IL-10+SPA* eEVs showed a significant decrease in IL-6 and TNFα secretion both at 3- and 6-h post-treatment (Figure 2D and Figure S3C, Supporting Information).

For cotreatment experiments, cells treated with LPS + *IL-4+SPA* eEVs or LPS + *IL-10+SPA* eEVs showed a significant reduction in *IL-6* expression after 3 and 12 h of cotreatment, and in the expression of *IL-1β* after 3 h of cotreatment compared to controls (Figure 3C and Figure S4A, Supporting Information). Moreover, cells treated with *IL-4+SPA* eEVs also showed a significant reduction in *TNF-α* expression after 12 h of cotreatment compared to controls, while cells treated with *IL-10+SPA* eEVs showed a reduction in *iNOS* expression after 12 h of cotreatment compared to controls (Figure S4A, Supporting Information). In terms of protein expression, *IL-4+SPA* eEV-treated cells showed a significant decrease in the secretion of IL-1β after 3 h of
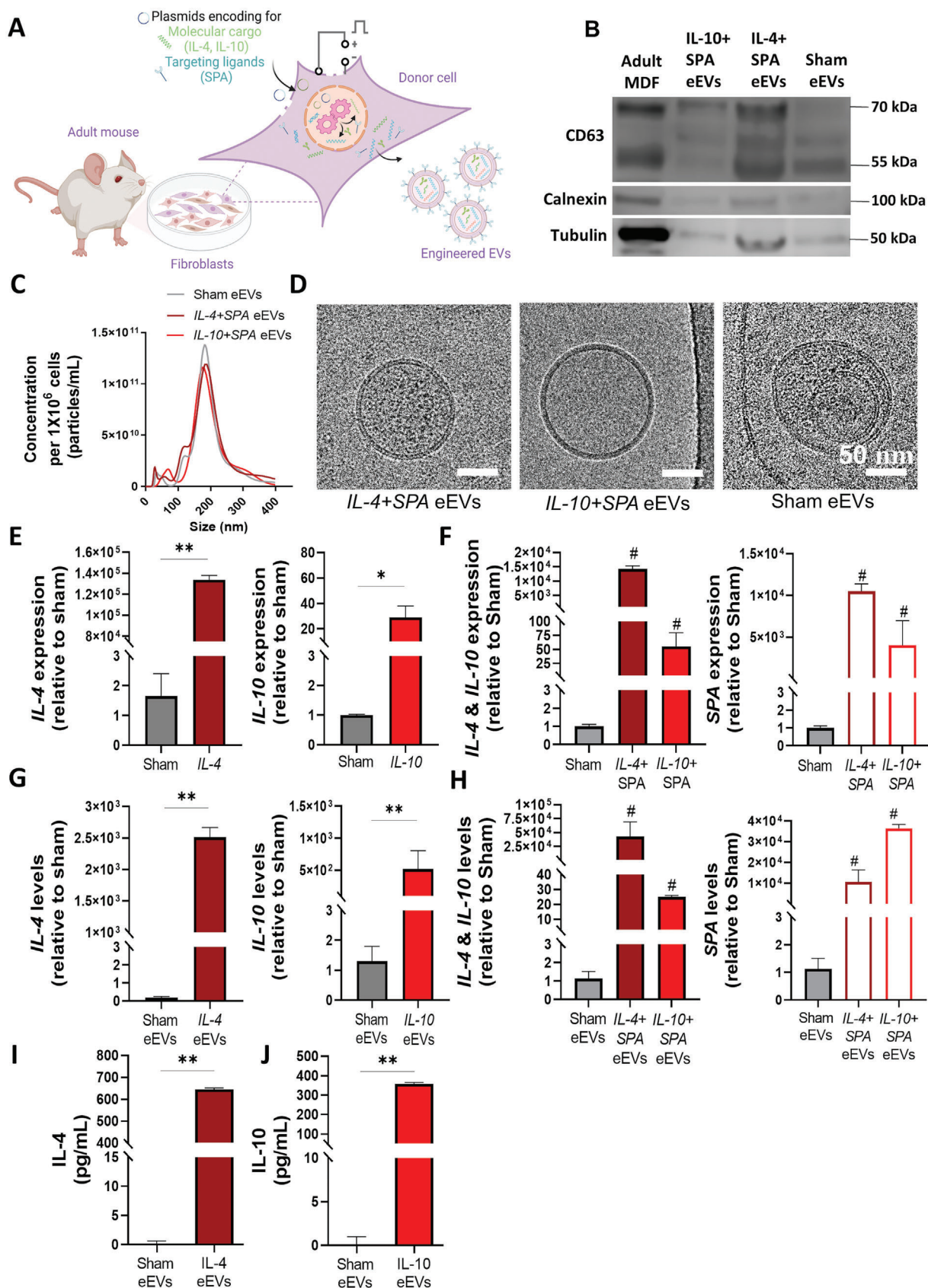
cotreatment compared to controls (i.e., LPS group) (Figure 3D). Cells treated with *IL-10+SPA* eEVs showed a significant decrease in IL-6 secretion after 3 and 12 h of cotreatment compared to controls (Figure 3D and Figure S4B, Supporting Information). In addition, cells treated with *IL-10+SPA* eEVs also showed a significant decrease in TNFα expression after 12 h of cotreatment compared to controls (Figure S4B, Supporting Information). In terms of morphology, LPS-challenged cells cotreated for 3 h with *IL-4+SPA* or *IL-10+SPA* eEVs showed a significant decrease in the percentage of activated monocytes compared to controls (Figure 3B). In addition, we also evaluated the effect of low, medium, and high eEV doses on macrophage responses. We observed that the dose can have an impact in the response of treated macrophages, where lower doses of eEVs seem to have a more beneficial effect on inflammation (Figure S5, Supporting Information). However, this finding could also be reflecting the effect of the increased nanoparticle load on macrophage activity.[55]

2.3. Decoration of eEVs with SPA-Targeting Ligand Leads to Enhanced Intrapulmonary Retention and Improved Overexpression of the Target Therapeutic Cargo

To increase the interactions with lung tissue and maximize intrapulmonary retention while minimizing liver clearance, eEVs were functionalized with SPA to promote binding with the P63/CKAP4 receptor on type II alveolar pneumocytes, which are key modulators of inflammation in the lung.[56,57] The presence of the functionalizing ligand SPA on the membrane of intact eEVs was confirmed via ELISA using intact eEVs (**Figure 4**A). The ability of the SPA-functionalized eEVs to preferentially accumulate in the lung was assessed in vivo using fluorescently labeled *IL-4+SPA* or *IL-10+SPA* eEVs delivered intranasally in 9-15-week-old male mice (Figure 4B). Biodistribution analysis conducted via IVIS at 12 h after delivery showed improved retention of SPA-functionalized eEVs in the lungs compared to nonfunctionalized (i.e., sham) eEVs (Figures 4C). Fluorescence microscopy analyses of lung tissue sections further revealed robust interaction and retention of the SPA-functionalized eEVs by lung cells (Figure 4D and E) compared to nonfunctionalized/sham eEVs. Effective transfection and overexpression of the target cargo in recipient cells in the lung were confirmed via 3,3′-diaminobenzidine (DAB) staining, as shown in Figure 4F,G.

2.4. SPA-Functionalized eEVs Loaded with *IL-4* and *IL-10* Dampen LPS-Induced Lung Inflammation In Vivo

To assess the efficacy of eEVs in dampening inflammation in vivo, we first established and characterized a model of acute lung injury via intranasal delivery of 0–4 mg kg^{-1} LPS to 9–10-week-old male mice (Figure S6A, Supporting Information). Lung injury parameters, including abnormal BALF (i.e., altered differential cellular counts, and increased protein and cytokine content), and secretion of proinflammatory mediators within the lung tissue, were then evaluated in response to the LPS challenge. Total protein content measurements in BALF revealed elevated protein levels for mice challenged with 0.4 or 4 mg kg^{-1} LPS compared to controls without LPS challenge, which potentially correlates with compromised integrity of the alveolar-capillary barrier and associated protein leakage into the alveolar space (Figure S6B, Supporting Information). Moreover, protein expression analysis conducted via ELISA showed a significant increase in the secretion of key proinflammatory mediators (i.e., IL-6, IL-1β, TNF-α) (Figure S6C, Supporting Information), with a robust increase in the recruitment of neutrophils and decreased macrophage recruitment compared to controls (Figure S6D,E, Supporting Information). Additionally, qRT-PCR analyses of lung tissue showed successful upregulation of the proinflammatory mediators IL-6, TNF-α, and iNOS for LPS-challenged mice (Figure S6F, Supporting Information).

Once we established a model of LPS-mediated acute lung injury, we set to test the therapeutic effect of *IL-4+SPA* and *IL-10+SPA* eEVs in mice challenged with 0.4 mg kg^{-1} of LPS. Intranasal delivery of eEVs was conducted 6 h after the LPS challenge, and the animals were euthanized after 12 h (**Figure 5**A). Our results showed a marked reduction in neutrophil recruitment in mice treated with *IL-4+SPA* or *IL-10+SPA* eEVs compared to mice treated with sham eEVs (Figures 5B,C). Furthermore, we observed a significant increase in macrophage recruitment for animals treated with *IL-10+SPA* eEVs in comparison with animals without eEV treatment (i.e., LPS group) (Figure 5B,C). We also found a trend toward decreased BALF protein content compared to LPS-challenged mice without eEV treatment, with robust attenuation in mice treated with *IL-10+SPA* eEVs (Figure 5D). ELISA analyses revealed a significant decrease in the secretion of the proinflammatory mediators IL-6, IL-1β, and TNF-α, in the lungs of mice treated with *IL-4+SPA*

Figure 1. Nonviral electrotransfection of dermal fibroblasts with IL-4, IL-10, and SPA leads to the release of eEVs loaded with IL-4, IL-10, and SPA. A) Schematic diagram illustrating the transfection of donor cells with plasmids encoding for molecular cargo (*IL-4 and IL-10*) and targeting ligand (SPA), and the generation of eEVs packed and functionalized with episomally expressed plasmids. Created using Biorender.com. B) Western blot analysis confirmed the presence of the EV marker, CD63 in *IL-10+SPA*, *IL-4+SPA*, sham eEVs, and donor cells. Moreover, the tubulin maker (cell cytoskeleton protein) was found in the donor cells and all eEVs formulations, and the protein calnexin (endoplasmic reticulum related) was detected in the donor cells and to a lesser extent in the eEVs. C) The NanoSight plot shows uniform and narrow distribution across the different groups in terms of concentration and size, with a peak at ≈200 nm ($n = 3$). D) Cryo-electron micrograph of *IL4+SPA*, *IL-10+SPA*, and sham eEVs revealed an intact structure. E) qRT-PCR analysis displaying the gene expression (mRNA transcripts) of the molecular cargo (*IL-4 or IL-10*) into adult-MDFs donor cells compared to sham-transfected cells ($n = 3$). F) Donor cells co-transfected with the molecular cargo (*IL-4 or IL-10*) and the targeting ligand (SPA) showing gene expression (mRNA transcripts) via qRT-PCR compared to sham-transfected cells ($n = 3$). G) qRT-PCR showed that the levels of *IL-4* and *IL-10* mRNA loaded inside eEVs was ≈2-3 order of magnitude higher compared to sham EVs ($n = 3$). H) The levels of the molecular cargo packed inside the eEVs were altered when the donor cells were co-transfected with *SPA* (*IL-4+SPA* or *IL-10+SPA* eEVs), where the expression of *IL-4* was found to be one order of magnitude higher with low expression of *SPA*, and *IL-10* was one order of magnitude lower with high expression of *SPA*. ELISA results of the I) IL-4 and J) IL-10 protein content associated with the eEVs compared to that in sham eEVs ($n = 3$). All error bars are shown as standard error of the mean (S.E.M.). *$p < 0.05$ and **$p < 0.001$, #significant difference with respect to the control with a p-value<0.05, One-way ANOVA and two-tailed *t*-test when appropriate.

**ADVANCED
SCIENCE NEWS**

www.advancedsciencenews.com

**ADVANCED
MATERIALS**

www.advmat.de
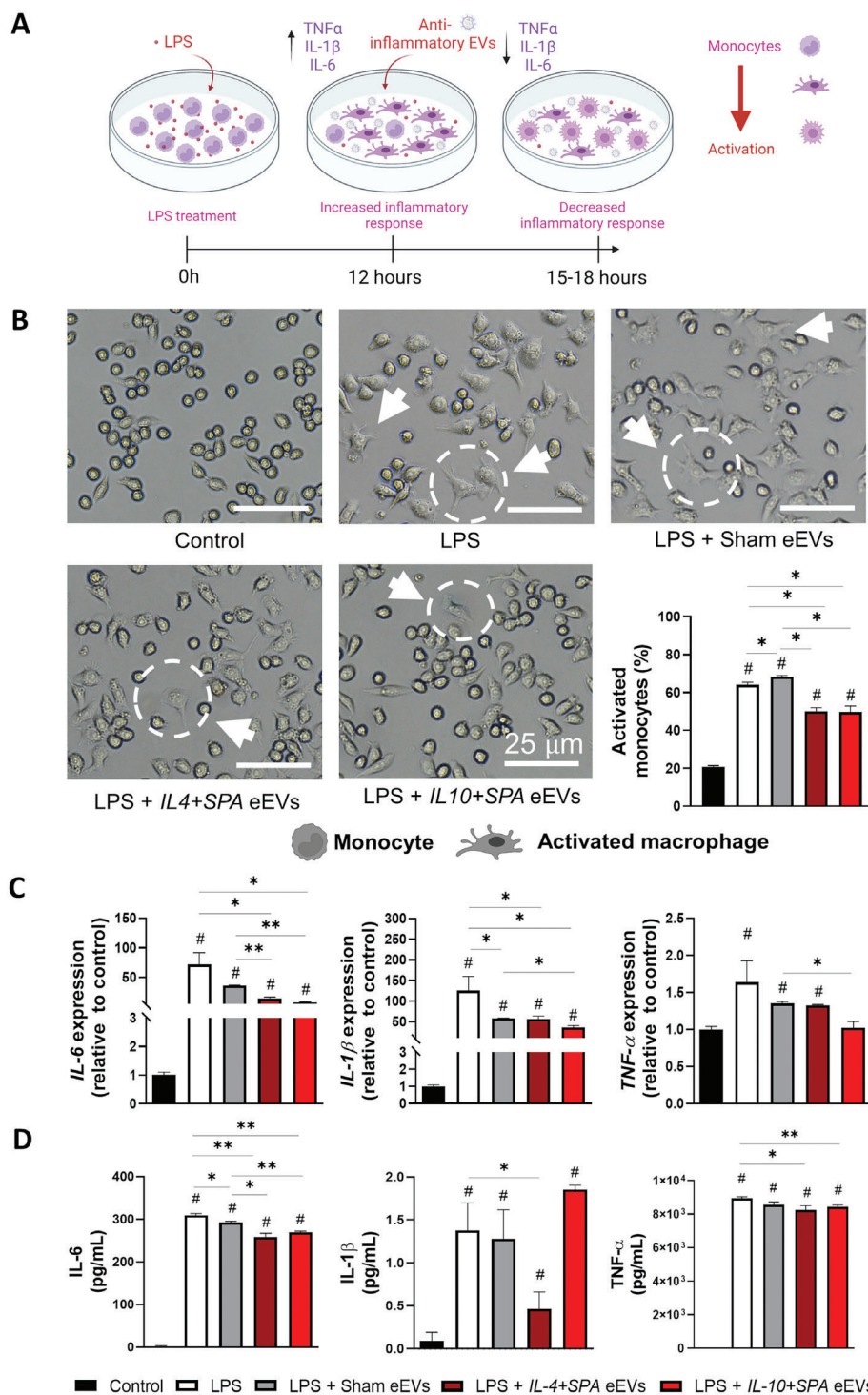
Figure 2. Early post-treatment (3 h) with *IL-4+SPA* and *IL-10+SPA* eEVs resolves activation and inflammation in LPS-challenged monocytes. A) Schematic representation of the inflammatory response driven by RAW 264.7 monocyte cultures in vitro when treated with the endotoxin lipopolysaccharide (LPS), and the therapeutic effect of the post-treatment with anti-inflammatory eEVs to dampen the induced inflammation. Created using Biorender.com. B) Representative microscopy images illustrating changes in cell morphology revealed that nontreated rounded monocytes get activated by the addition of the LPS, transitioning into a spindled shape typical of an activated or differentiated macrophage. Quantification analyses indicate that cell cultures treated with *IL-4+SPA* and *IL-10+SPA* EVs have less activated monocytes compared to the LPS and sham eEV groups. C) qRT-PCR analyses showed increased expression of *IL-6, IL1-β,* and *TNF-α* compared to the control (no LPS), and a decreased expression of *IL-6,* and *IL1-β* when treated with *IL-4+SPA* and *IL-10+SPA* eEVs. D) IL-6 and TNF-α protein expression was reduced when treated with both eEVs and IL1-β with just *IL-4+SPA* eEVs (n = 3). All error bars are shown as S.E.M. *p < 0.05 and **p < 0.001, #significant difference with respect to the control with a p-value < 0.05, one-way ANOVA.
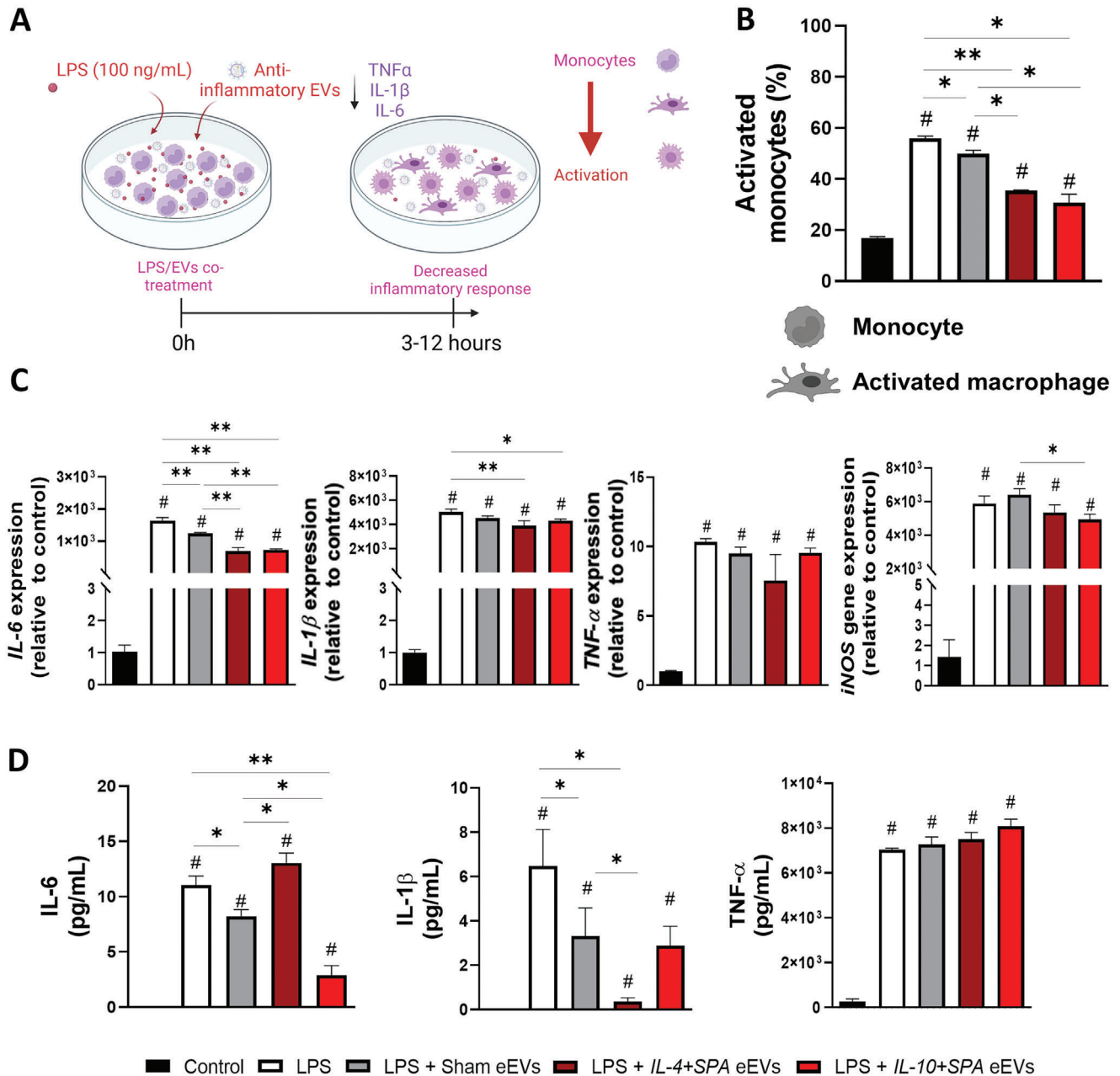
Figure 3. Early cotreatment (3 h) with *IL-4+SPA* and *IL-10+SPA* eEVs resolves activation and inflammation in LPS-challenged monocytes. A) Schematic representation of the therapeutic effect of the co-treatment of RAW 264.7 monocytes with LPS and the anti-inflammatory eEVs to dampen inflammation. Created using Biorender.com. B) The percentage of activated monocytes (spindle shape) was reduced when treated with *IL-4+SPA*, *IL-10+SPA*, and sham eEVs. C) qRT-PCR analysis showing the expression of proinflammatory cytokines for the LPS group compared to the control, and the reduction in *IL-6*, *IL1-β*, and *iNOS* expression when treated with *IL-10+SPA* eEVs, and in *IL-6* when treated with *IL-4+SPA* eEVs. D) At the protein level, IL-6 expression decreased when treated with *IL-10+SPA* eEVs and IL1-β when treated with *IL-4+SPA* ($n = 3$). All error bars are shown as S.E.M. *$p < 0.05$ and **$p < 0.001$, #significant difference with respect to the control with a *p*-value < 0.05, One-way ANOVA.

or *IL-10+SPA* eEVs compared to mice without eEV treatment (Figure 5E).

Tissue injury in terms of altered lung morphology was evaluated using hematoxylin and eosin-stained lung sections (Figure 5F). This lung tissue morphometric analysis revealed a significant reduction in the degree of tissue injury after LPS-challenge for animals treated with *IL-4+SPA* and *IL-10+SPA*

eEVs, with an increased number of alveoli per high power field (hpf) (Figure 5G), and a reduced mean septal thickness and mean linear intercept (MLI) (Figure 5H,I), compared to nontreated (i.e., LPS group) and sham eEVs-treated animals. Additionally, measurements including elastance, compliance, resistance of respiratory system, tissue elastance, tissue damping, and inspiratory capacity, are included in Figure S7 (Supporting Information).

ADVANCED
SCIENCE NEWS

www.advancedsciencenews.com

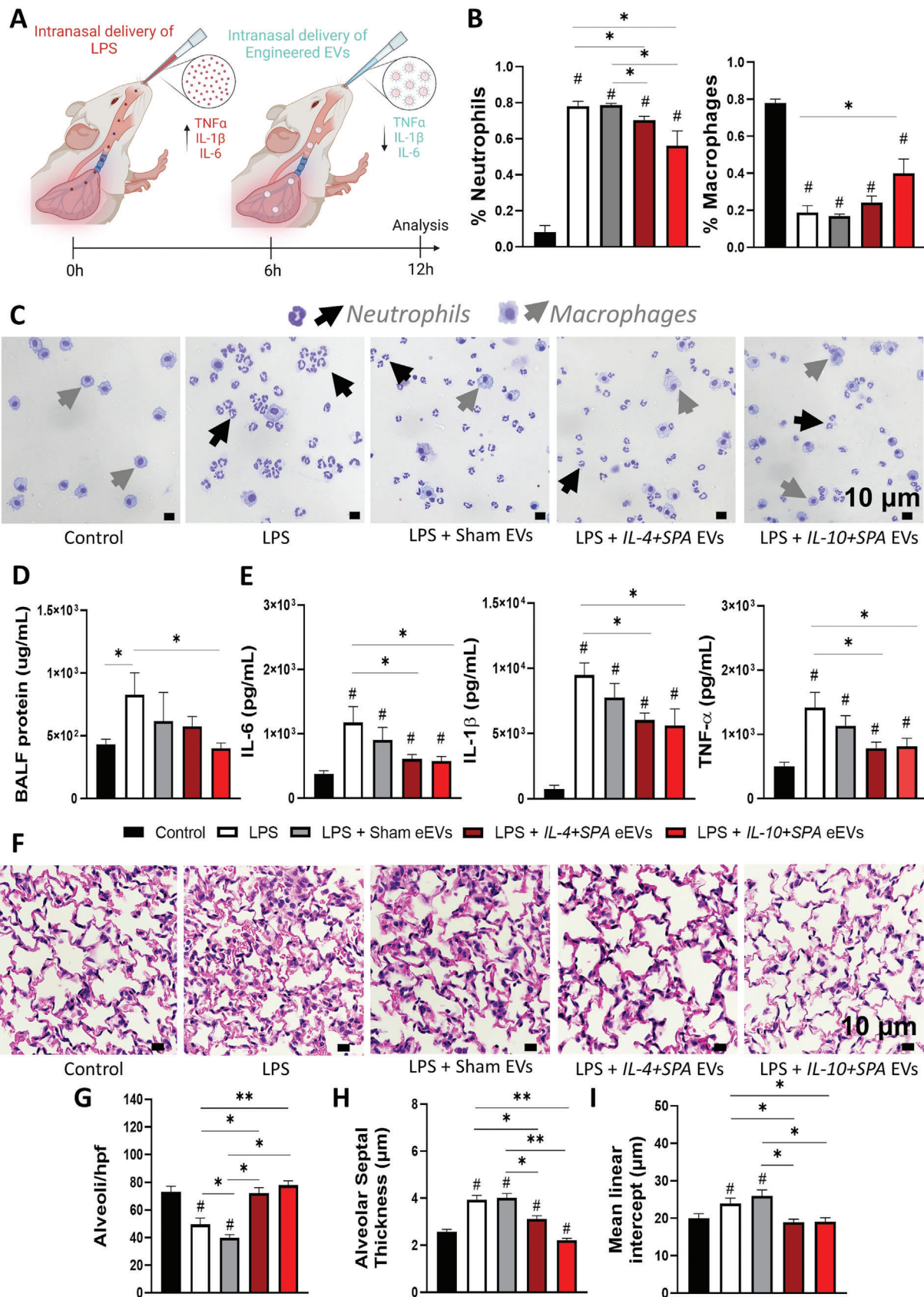**ADVANCED**
MATERIALS

www.advmat.de
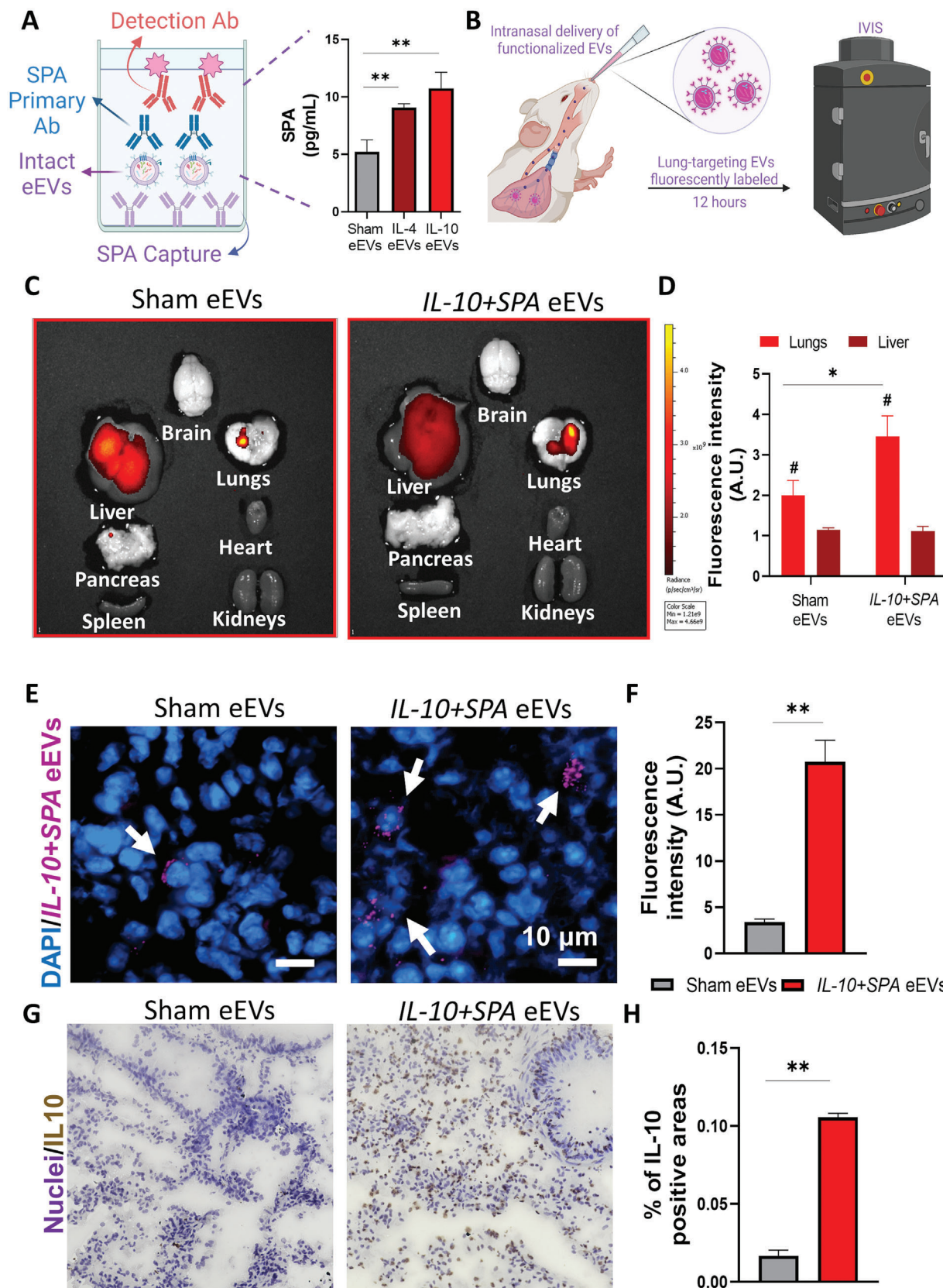
2.5. Untargeted Metabolomics Analysis Reveals Differential Metabolic Profiles in the BALF of LPS Challenged Mice Treated with *IL-4+SPA*, *IL-10+SPA*, and Sham eEVs

An untargeted metabolomics analysis was conducted to identify metabolic changes driven by treatment with the different eEVs formulations in mice with induced acute lung inflammation. For this analysis, BALF samples were collected from LPS-challenged mice (LPS), healthy mice (control), and LPS-challenged mice treated with *IL-4+SPA*, *IL-10+SPA*, or sham eEVs (sham). The liquid chromatography with tandem mass spectrometry (LC-MS/MS) in positive and negative ionization modes revealed 3308 features. Prior to multivariate and univariate statistical analyses, data normalization was performed using auto-scaling (mean-centered, divided by the standard deviation of each variable) and log transformation (Figure S8, Supporting Information). Unsupervised and supervised data dimensionality reduction approaches were first used to explore all the data (Figure S9, Supporting Information). Principal component analysis (PCA) was employed to visually discriminate the samples, however, the variance in the dataset explained by PC1 and PC2 showed partial separation (Figure S9A,B, Supporting Information). Partial-least-squares discriminant analysis (PLS-DA) showed better clustering of the four groups (Figure S9C,D, Supporting Information). Cross validation showed that 5 components were optimal for building the model and the permutation test ($n = 2000$) with a *p*-value lower than 0.05, indicating that PLS-DA showed a good predictive model (Figure S9E–H, Supporting Information). After performing a pairwise comparison of the LPS group against all other groups, using the supervised PLS-DA approach, a clear separation between the groups was observed, indicating differential metabolomic profiles between the LPS-challenged mice and the healthy controls, and between the LPS-challenged mice and all the eEVs treatment groups (**Figure 6**A–D and Figure S10A–D, Supporting Information). Features with an FDR < 0.1, foldchange > 2, and Variable Importance in the Projection (VIP) score > 1.0 were considered significantly different between groups (Table S5, Supporting Information). When samples from healthy controls were compared to samples from mice challenged with LPS, 82 features were upregulated in the control, while 31 were downregulated. Compared to LPS-challenged mice, BALF from the *IL-4+SPA* eEV-treated mice, showed the downregulation of 33 features, with the same number of features being upregulated; while for the *IL-10+SPA* eEV-treated mice, 27 features were upregulated and 14 were downregulated. On the other hand, for

sham eEV-treated mice, 106 features were upregulated while 15 were downregulated (Figure 6, Figure S10, Supporting Information, and Table S5, Supporting Information). From the set of features that were significantly up/downregulated, only the annotated metabolites that are presented in **Figure 7**A were further explored. 2″-Deoxycytidine 5″-monophosphate, malic acid, *N*-phenylacetylglycine, 15-methylpalmitate, heptanoylcarnitine, and fenofibrate, were among the features determined to be statistically increased between LPS-challenged animals and healthy animals (i.e., control group). Interestingly, ascorbic acid and oxoglutarate were both found to be significantly upregulated in the BALF of animals treated with *IL-4+SPA* and *IL-10+SPA* eEVs, while tryptophan was significantly downregulated in both groups (Figure 7A). For the *IL-4+SPA* eEV-treated mice, upregulation of the monosaturated fatty acid 7-heptadecenoic acid, and downregulation of phenylalanine, isoleucine/leucine, and tyrosine were observed. While for the *IL-10+SPA* eEV-treated mice, phosphodimethylethanolamine, adenosine, inosine, 8E-heptadecenedioic acid, and dodecanoyl-L-carnitine were upregulated, while the triglycerides TG(52:0) and TG(34:0) were downregulated. For the sham eEV-treated group, several other metabolites were upregulated, including uridine, citric acid, vitamin K, glucuronic acid, ubiquinone 6, cortisone, and linoleic acid, among others. The metabolite 9-(2,3-dihydroxypropoxy)-9-oxononanoic acid was increased in BALF samples of animals treated with both, sham and *IL-10+SPA* eEVs. While 7-heptadecenoic acid was increased in BALF samples from animals treated with sham and *IL-4+SPA* eEVs.

Pathway analysis comparing BALF samples obtained from LPS-challenged mice vs eEVs-treated mice revealed an increase in the TCA cycle for animals treated with eEVs (*IL-4+SPA*, *IL-10+SPA*, and sham), while treatment with *IL-4+SPA* and *IL-10+SPA* eEVS caused an increase of urea cycle and the metabolism of arginine, proline, glutamate, aspartate, and asparagine. Purine metabolisms were increased upon treatment with *IL-10+SPA* eEVS. Treatment with sham eEVs caused the upregulation of other distinct pathways including those of linoleate, histidine, vitamin K, ubiquinone, C21-hormone biosynthesis, glycosphingolipid, pyrimidine, de novo fatty acid biosynthesis, among others (Figure 7B). *IL-4+SPA* and sham eEVs caused an increase in the glycerophospholipid pathway, while treatment with *IL-10+SPA* eEVs caused a decrease in this pathway. Moreover, tryptophan metabolism was downregulated in *IL-4+SPA* and *IL-10+SPA* eEV-treated animals. Tyrosine and biopterin metabolism and the degradation of valine, leucine, and isoleucine were decreased in *IL-4+SPA* eEV-treated animals.

Figure 4. SPA functionalized anti-inflammatory eEVs with improved lung retention and accumulation. A) Schematic representation of the detection of SPA protein on the surface of the eEVs and data showing the successful transfer of the episomally expressed ligand SPA to the surface of the eEV membrane confirmed via ELISA compared to sham EVs. B) Schematic diagram illustrating the intranasal delivery of fluorescently labeled lung-targeting eEVs and analysis using an in v*ivo* imaging system (IVIS) 12 h after delivery. A,B) Created using Biorender.com. C) IVIS images of major organs showing accumulation of the eEVs in the lungs, with higher retention when treated with SPA-functionalized *IL-10+SPA* eEVs compared to nonfunctionalized (sham) eEVs, and D) comparative analysis of the fluorescence radiant efficiency units to quantify eEV accumulation. E) Immunofluorescence images of lung tissue samples after IVIS of animals treated with fluorescently labeled (Far-Red) sham and *IL-0+SPA* eEVs co-localized with the nuclei of the cells in blue (DAPI), 12 h after intranasal delivery (arrows pointing at positive cells). F) Respective fluorescence intensity quantification of 4 lung tissue sections per animal. Scale bar: 10 µm. G) DAB staining images showing the positive expression of IL-10 in the lungs of animals treated with *IL-10+SPA* eEVs compared to sham eEVs, this signal was co-localized with the nuclei of the cells. H) Quantification of IL-10 expression (% of positive areas) in the lung tissue showing overexpression of IL-10 in the *IL-10+SPA* eEV-treated group compared to the sham eEV-treated group ($n = 4$). All error bars are shown as S.E.M. *$p < 0.05$ and **$p < 0.001$, #significant difference with respect to the control with a *p*-value < 0.05, one-way ANOVA, or two-tailed *t*-test when appropriate.

**ADVANCED
SCIENCE NEWS**

www.advancedsciencenews.com

**ADVANCED
MATERIALS**

www.advmat.de

**ADVANCED
SCIENCE NEWS**

www.advancedsciencenews.com

**ADVANCED
MATERIALS**

www.advmat.de

Sham eEVs on the other hand, caused a downregulation of the phosphatidylinositol phosphate metabolism (Figure 7B). Our results show that the metabolic profiles in BALF samples of LPS-challenged mice are clearly impacted by treatment with eEVs loaded with *IL-4+SPA* or *IL-10+SPA*, but also significantly different than that caused upon treatment with sham eEVs. Overall, we were able to see that different metabolomic responses are elicited depending on the molecular payload of the eEVs.

3. Discussion

To the best of our knowledge, this is the first report describing the implementation of dermal fibroblasts as donor cells to derive eEVs loaded with anti-inflammatory cargo and functionalized to preferentially target the lung tissue. In recent years, EVs derived from progenitor cells (e.g., endothelial progenitors, and mesenchymal stem/stromal cells) have been postulated as an effective alternative to cell-based therapies.[58] For example, EVs derived from mesenchymal stem cells (MSCs) have been extensively explored for the treatment of pulmonary diseases due to their ability to restore epithelial cell integrity and function and to reduce inflammation during lung injury.[37,39,59] Numerous studies have reported that MSC-derived EVs are loaded with multiple effector molecules, including anti-inflammatory cytokines, growth factors (e.g., KGF), and antimicrobial peptides.[22,58,60] Progenitor cell-derived EVs, however, still face multiple hurdles, including limited cell sources and increased risk for tumorigenicity and immunogenicity. Our results suggest that dermal fibroblasts-derived EVs could potentially circumvent many of these barriers, not only because dermal fibroblasts represent a viable and more abundant and readily available source of EVs, but also due to their reduced immunogenicity likely driven by decreased expression of the major histocompatibility complex (MHC) on their surface.[61] Moreover, dermal fibroblasts are currently being used in clinical applications for dermal grafts, which highlights their potential to be a promising cell source for EV-based therapeutics.[62–65]

EVs have been shown to have a therapeutic potential to modulate inflammation in several clinical disorders.[66–68] Their pro- and anti-inflammatory properties can be attributed to the presence of cytokine components exposed on their membrane and/or packed in their lumen, working synergistically.[40,69] Previous studies have shown that cytokines such as IL-4, IL-10, IL-2, IL-12, and IL-16 are preferentially packed within the EVs, while IL-8, IL-17, and GRO-*α* are mostly found on the EV surface.[69,70] Taking advantage of this 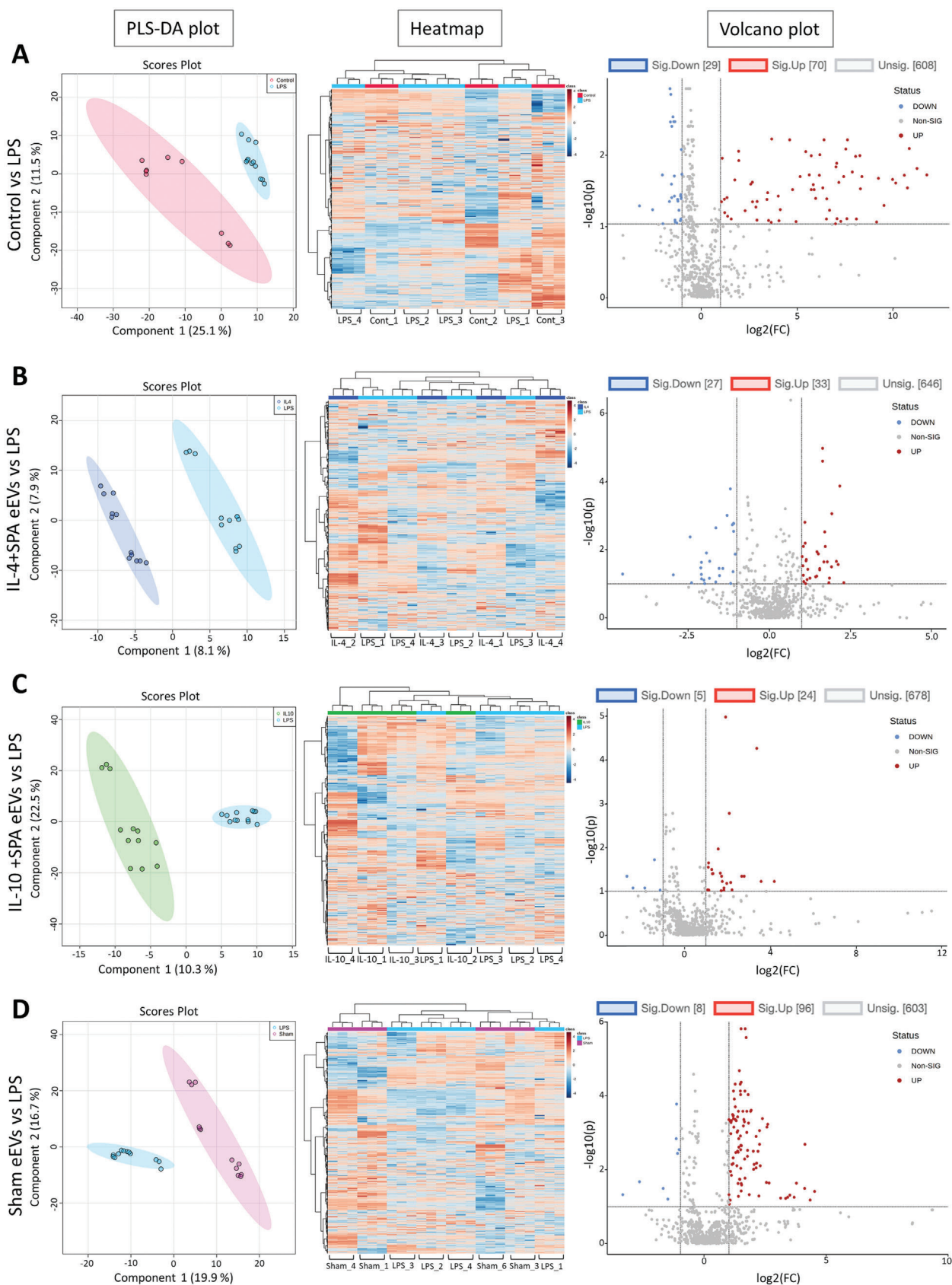predisposition to pack cytokine components, we proposed the implementation of *IL-4* and *IL-10* as model anti-inflammatory cargo. Moreover, *IL-4* and *IL-10* have well-documented properties to reduce the inflammation and mortality associated with ARDS.[23,71] *IL-10* released by activated macrophages and Th1 cells is known to be involved in the reduction of proinflammatory cytokines by downregulation of Th1 cells and inhibiting the production by alveolar macrophages of proinflammatory mediators (e.g., TNF-*α*, IL-1*β*, IL-6, Interferon ϒ) involved in ARDS.[10,20,72,73] On the other hand, *IL-4* possesses immunosuppressive and anti-inflammatory properties mediated by the inhibition of key proinflammatory mediators (e.g., TNF-*α*, IL-1*β*, IL-6, IL-12, IL-8) and plays an important role on the differentiation of CD4+ T cells to Th2 cells and monocytes into macrophages.[72,74–76] Additional studies have reported that endogenous and exogenous *IL-4* are implicated in the late resolution of lung inflammation by promoting polarization of monocytes toward an anti-inflammatory phenotype (M2) and neutrophil clearance, which dampens inflammation and enhances lung repair.[93]

Our results highlight the ability of dermal fibroblast-derived eEVs to safely and selectively package mRNA transcripts of the electrotransfected anti-inflammatory cargo, reaching loading levels that are 2–6 orders of magnitude higher compared to eEVs derived from sham-transfected dermal fibroblasts. Additionally, we also verified that besides DNA and mRNA, there is also IL-4 and IL-10 protein content associated with the EVs. Characterization of the eEVs showed that morphology, size distribution, and membrane protein content were consistent with the standards issued by the International Society for Extracellular Vesicle guidelines.[77] Our results also demonstrate the ability of eEVs to effectively transduce recipient cells in the alveolar environment to trigger overexpression and secretion of *IL-4* and *IL-10*, via effective delivery of mRNA transcripts and plasmid DNA encoding for these cytokines. Although our results provide robust preclinical data supporting the therapeutic efficacy and safety of *IL-4* and *IL-10* engineered EVs using a murine model of acute lung inflammation, additional studies are needed to look at toxicology, safety, and efficacy in larger animal models before this technology can be translated into the clinic.

EV-based payload delivery systems offer a promising cell-free therapy, with a highly customizable platform that can potentially be engineered to maximize targeted delivery, of anti-inflammatory therapies for lung injury. This type of targeted delivery enables the implementation of lower doses, with limited off-target systemic effects, which maximizes therapeutic efficacy. While EVs have been shown to have inherent targeting character-

Figure 5. SPA-functionalized eEVs loaded with *IL-4* and *IL-10* dampen LPS-induced lung inflammation and tissue damage in vivo. A) Schematic diagram depicting the experimental timeline of the intranasal delivery of 0.4 mg kg^{-1} LPS that elicits an inflammatory response (0 h), treatment with anti-inflammatory eEVs delivered intranasally (6 h), and subsequent analysis to evaluate lung injury parameters (12 h). Created using Biorender.com. B,C) Differential cellular counts showing reduced neutrophils recruitment in bronchoalveolar lavage fluid (BALF) for animals treated with *IL-4+SPA* eEVs (≈70%), and *IL-10+SPA* eEVs (≈60%) compared to LPS-challenged mice without treatment (≈80%). D) BALF analysis shows a decreased amount of total protein concentration for animals treated with *IL-10+SPA* eEVs compared to LPS-challenged mice without treatment. E) Lung tissue protein analysis via ELISA displaying decreased expression of IL-6, IL1-*β*, and TNF-*α* for animals treated with *IL-4+SPA* and *IL-10+SPA* eEVs with respect to the LPS-challenged mice without treatment. F) Representative microscopy images of hematoxylin-and-eosin-stained lung sections at 90× magnification used for lung tissue morphometric analysis showing a significantly higher number of alveoli per hpf (high power field) (G), decreased alveolar septal thickness (H), and mean linear intercept (MLI) (I) for animals treated with *IL-4+SPA* or *IL-10+SPA* eEVs, compared to LPS-challenged mice without treatment and sSham eEV-treated mice (n = 4). All error bars are shown as S.E.M. *$p < 0.05$ and **$p < 0.001$, #significant difference with respect to the control with a *p*-value < 0.05, one-way ANOVA.

**ADVANCED
SCIENCE NEWS**

www.advancedsciencenews.com

**ADVANCED
MATERIALS**

www.advmat.de

istics and display tropism for particular cells or tissues,[78,79] they can also be modified with ligands (e.g., integrins, protein ligands, peptides, nucleic acids) to facilitate the targeting/recognition of specific receptors for preferential binding and payload delivery, avoiding major off-target effects.[43,80–82]

Type II pneumocytes constitute 60% of alveolar epithelial cells and make up 10–15% of all cells present in the lungs.[83] The relevance of this is that alveolar epithelial cells are the first line of cells that secrete proinflammatory mediators (e.g., cytokines, chemokines) in response to pathogenic/harmful stimuli, leading and orchestrating the recruitment of innate and adaptative immune cells to the site of injury and/or infection.[84,85] Our results show that the targeting ligand SPA improved intrapulmonary retention of the eEVs with reduced liver clearance and facilitated localized delivery of anti-inflammatory payloads. SPA interacts with the receptor P63/CKAP4 on alveolar pneumocytes[56] and can also bind to Toll-like Receptor-2 (TLR2),[57] potentially dampening the activation of the $NF\kappa\beta$ inflammatory pathway and macrophage activation.[52] SPA has also been shown to decrease proinflammatory mediators on LPS-stimulated alveolar macrophages by binding to INF-Y and preventing the interaction between INF-ϒ and its receptor INF-ϒR.[52] Furthermore, SPA/P63 interaction is implicated in the reduction of alveolar surface tension and prevention of alveoli collapse.[56,86] In addition, qRT-PCR characterization revealed that eEVs also carry mRNA transcripts of SPA (Figure 1H), which could potentially bolster local SPA expression and may further attenuate lung inflammation due to its role in maintaining immune homeostasis in the lung microenvironment.[52]

The most common models of ARDS included the administration of endotoxin (LPS),[87,88] acid aspiration,[89,90] prolonged hyperoxia,[91] mechanical ventilation with low tidal volumes,[92,93] ischemia/reperfusion,[94] and airway installation of live bacteria or influenza virus,[95] which can cause damage of the pulmonary vascular endothelium and/or bronchoalveolar epithelium.[79,80] Here we ran a comprehensive study looking into the entire process, involving the dynamics, optimal concentration, and treatment method (co- or post-treatment), of the inflammatory response mounted by LPS in vitro and in vivo expanding on previous reports[87,88,96] (Figures S2 and S6, Supporting Information). Moreover, we confirmed the feasibility of using LPS to simulate an inflammatory response in vivo, to test the therapeutic effect of the eEVs. A suitable in vivo model of ARDS has to meet some basic criteria, including accumulation of neutrophils in the alveolar/interstitial space, an increase of protein concentration in BALF representative of the disruption of alveolar-capillary barrier, an increase of proinflammatory mediators in lung tissue or BALF, and physiological changes consistent with pulmonary dysfunction, in accordance with guidelines from the American Thoracic Society (ATS).[97,98] Our results show that our in vivo model induces this type of inflammatory response, and it is responsive to treatment via eEVs. The expression of LPS-induced

inflammatory mediators (i.e., IL-6, IL-1β, and TNF-α) was consistently reduced in mice treated with *IL-4+SPA* and *IL10+SPA* eEVs. The observed differences are consistent with previous reports characterizing cytokine expression in patients with and without ARDS.[99] Additionally, lung tissue morphometric analysis revealed the potential of eEVs to aid tissue repair, where animals treated with *IL-4+SPA* or *IL-10+SPA* eEVs showed an increased number of alveoli per high power field (hpf), and a reduced mean septal thickness and mean linear intercept (MLI), compared to nontreated (i.e., LPS group) and sham eEV-treated animals.

In vitro experiments on the other hand show some potential effect of the sham eEVs to reduce some of these markers, but this effect was not consistent across the different treatment options evaluated (i.e., post- or cotreatment for 3–12 h). Moreover, this effect was not observed when testing the therapeutic effect of the different eEV formulations in vivo.

The untargeted metabolomics approach used in this study aimed at assessing the effect of treating LPS-challenged mice with anti-inflammatory dermal fibroblast-derived eEVs. Cluster separation of healthy controls versus LPS-treated mice indicates a robust change in the metabolomes of the collected BALF samples (Figure 6A, and Figure S10A, Supporting Information). The accumulation of heptanoylcarnitine in LPS-challenged mice, a derivative of O-acetylcarnitine, had previously been reported as part of the BALF metabolome of patients with acute lung injury.[100] Also, the statistically significant increase of 15-methylpalmitate and *N*-phenylacetylglycine was a distinguishing characteristic for LPS-challenged mice. The former compound is a long saturated fatty acid, which has been reported to have pro-inflammatory effects on macrophages.[101] Although the biological significance of the accumulation of phenylacetylglycine is unclear, its accumulation has been reported in the urine of patients with ischemic heart failure, as well as in the plasma of rats subjected to chronic cigarette smoke exposure.[102,103] Treatment of LPS-challenged mice with *IL-4+SPA*, *IL-10+SPA*, and sham eEVs caused changes in the BALF metabolome. However, the metabolic profiles of animals treated with *IL-4+SPA* and *IL-10+SPA* eEVs were more similar to each other than to the sham eEV-treated animals; as the sham eEV-treated mice clustered apart from *IL-10+SPA eEVs*, *IL-4+SPA eEVs*, and the healthy control, with some overlapping with the LPS group (Figure S9D, Supporting Information). Upon treatment with *IL-4+SPA* and *IL-10+SPA* eEVs, an upregulation of ascorbic acid and oxoglutarate occurred in the BALF of LPS challenged mice. Ascorbic acid (vitamin C) is a potent antioxidant that has been reported to provide protection against reactive oxygen species, preventing the damaging effects of oxidative stress, and it is also known for its anti-inflammatory role.[104,105] Previous studies have shown that ascorbic acid attenuates systemic inflammation induced by acute lung injury.[106] Likewise, oxoglutarate has been reported to have antioxidant properties and to play a key role in macrophage

Figure 6. Multivariate and univariate statistical analyses of the metabolomics dataset obtained in negative ionization mode. 2D score plot of partial squares discriminant analysis (PLS-DA) (left) showing the separation of each of the treatment groups and the LPS-challenged mice; heatmap showing hierarchical clustering obtained based on Euclidean distance (middle); and volcano plot of univariate statistical analysis showing significant values of the features in each treatment group in comparison with LPS-challenged mice, with fold change values >2 and false discovery rate (FDR) <0.1 (right). A) Healthy mice (Control) vs LPS-challenged mice, B) *IL-4+SPA* eEV-treated mice vs LPS-challenged mice, C) *IL-10+SPA* eEV-treated mice vs LPS-challenged mice, and D) sham eEV-treated mice vs LPS-challenged mice.
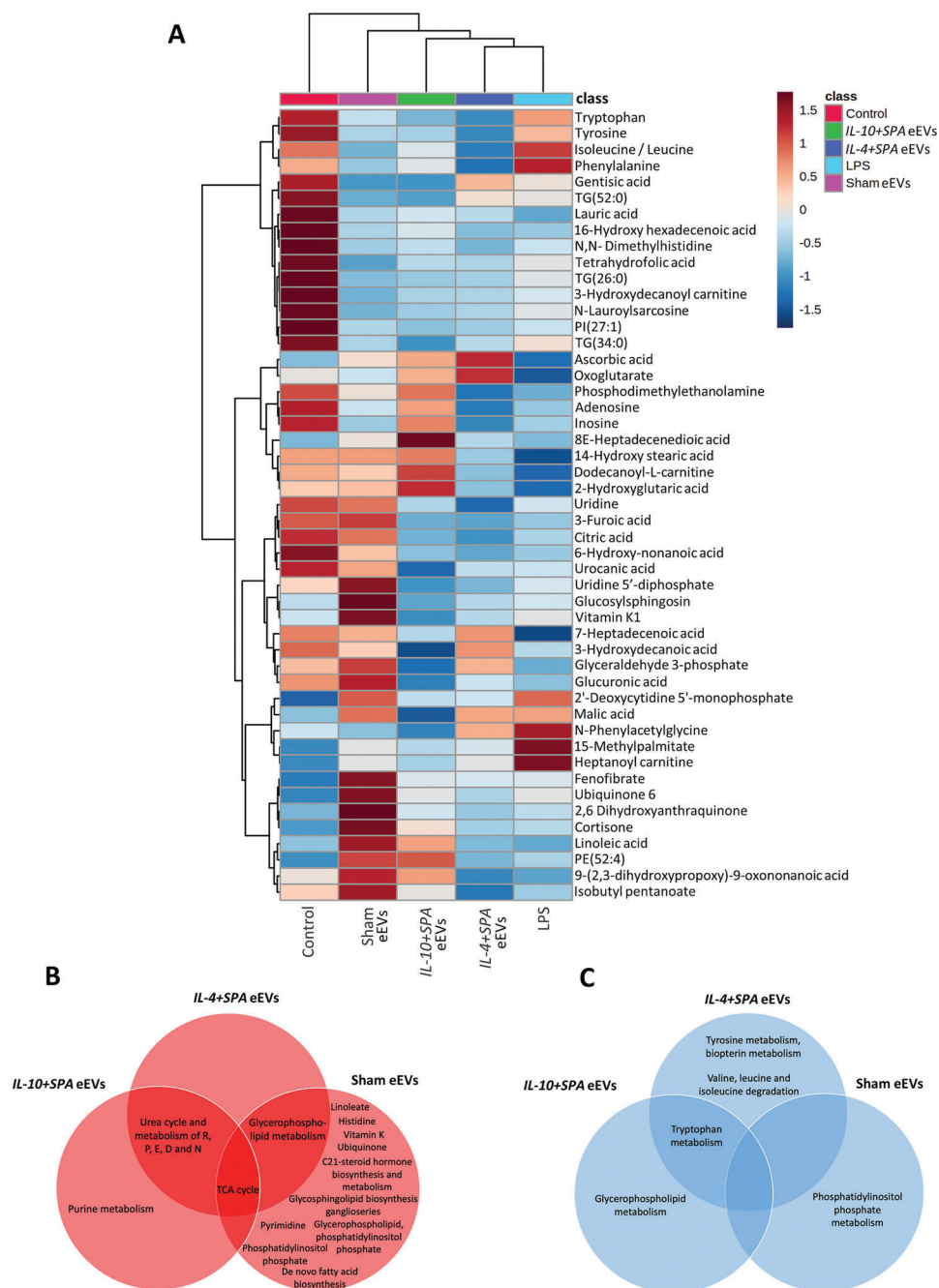
Figure 7. Heatmap of annotated metabolites collected from bronchoalveolar lavage fluid (BALF) of mice. A) Heatmap of the hierarchical cluster analysis showing the detected and annotated metabolites collected from the BALF of mice treated with 0.4 mg kg^{-1} LPS, treated with *IL-10+SPA*, *IL-4+SPA*, or sham eEVs. The control treatment group consists of BALF collected from healthy mice that were not exposed to LPS. The metabolites shown in this graph correspond only to the annotated features that had FRD > 0.1 and FC > 2 resulting from the comparison of each treatment group vs LPS-challenged mice, calculated using one-way ANOVA. The averages of 3 technical and 3–4 biological replicates are presented. Each colored cell on the map corresponds to a concentration value in the data table, with samples in rows and features/compounds in columns. B) Pathway analysis of upregulated pathways after treatment with *IL-4+SPA*, *IL-10+SPA*, or sham eEVs. C) Pathway analysis of downregulated pathways after treatment with *IL-4+SPA*, *IL-10+SPA*, or sham eEVs.

ADVANCED
SCIENCE NEWS

www.advancedsciencenews.com

**ADVANCED
MATERIALS**

www.advmat.de

polarization into an M2 anti-inflammatory phenotype.[107,108] Interestingly, these two metabolites were not significantly upregulated in any of the control groups, suggesting a potential involvement in the reduction of lung inflammation. Moreover, the upregulation of adenosine and inosine in the *IL-10+SPA eEV*-treated mice could also be an indication of the therapeutic effect of these eEVs, as these metabolites have also been reported to play a role in anti-inflammatory processes associated with acute lung disease.[109–112] Treatment with *IL-4+SPA* eEVs also showed to cause a significant reduction of phenylalanine in BALF; the increased accumulation of this amino acid in blood plasma has been described as a potential biomarker and as a mortality predictor for ARDS patients.[113] Furthermore, the metabolomic changes caused by the treatment with sham eEVs also resulted in the upregulation of certain metabolites with antioxidant or anti-inflammatory effects, including ubiquinone, citric acid, cortisone, uridine, and linoleic acid.[114–118] We also note that the results obtained from this untargeted metabolomics analysis provide relative abundances of the metabolites, hence the use of standards in future experiments will enable further assessment of the systemic levels of these metabolites and how they compare with known safe levels.[119,120] Overall, after assessing the effect of *IL-4-* and *IL-10*-loaded anti-inflammatory eEVs using an untargeted metabolomics approach, we were able to uncover changes in the metabolic profiles in the BALF of LPS-challenged mice, which paves the way to having a more complete understanding of the unexplored metabolic response of using eEVs as potential therapeutic agents. Our findings shed light on the potential mechanisms involved in the anti-inflammatory response upon treatment with the eEVs.

4. Conclusion

We describe an effective methodology to generate engineered (eEV)-based nanocarriers derived from primary adult mouse dermal fibroblasts. Our results highlight how SPA-decorated *IL-4-* or *IL-10*-loaded eEVs showed enhanced intrapulmonary retention, and can effectively deliver IL-4 and IL-10 transcripts and plasmid DNA to alveolar cells in the inflamed lung environment to boost the levels of these anti-inflammatory cytokines, mitigating the local inflammatory response. Although SPA decoration seems to improve intrapulmonary retention, by likely improved interactions with specific epithelial cell subpopulations in the lung based on ligand-receptor interactions, the main cellular target of the eEVs in the lung microenvironment must be further studied, as their significant therapeutic effect is likely due to the production of IL-4 and IL-10 by multiple types of recipient cells in the lung (e.g., macrophages and epithelial cells). Notably, we report that *IL-4+SPA* and *IL-10+SPA* eEVs have the ability not only to reduce the secretion of key proinflammatory mediators such as IL-6, IL-1β, and TNF-α, but also to aid tissue repair and to induce significant metabolomic changes to favor activation of anti-inflammatory pathways mediated in part by the significant upregulation of ascorbic acid, inosine, and oxoglutarate. These results establish the potential of using skin fibroblast-derived anti-inflammatory eEVs, obtained via nonviral approaches, to selectively deliver therapeutic payloads to the inflamed lung to reduce inflammation, tissue damage, and the prevalence/progression of lung injury during ARDS.

5. Experimental Section

DNA Plasmid Preparation: Plasmids used in this study (Table S1) were obtained from OriGene Technologies, prepared via bacterial transformation, and isolated using a ZymoPure II kit (Zymo Research) for plasmid DNA isolation, following the procedure described by the manufacturer. DNA concentrations and quality were measured using a Nanodrop 2000c Spectrophotometer (Thermo fisher Scientific).

In Vitro Cell Culture: Adult BALB/c mouse primary dermal fibroblasts (adult-MDFs) were obtained from Cell Biologics (BALB-5067) and cultured using complete fibroblast basal medium with the growth factor supplements provided by the vendor (Cell Biologics, M2267) and incubated at 37 °C in humidified air containing 5% CO_2 (standard culture conditions). Additionally, monocytes RAW 264.7, a transformed cell line derived from BALB/c mice, were obtained from ATCC (TIB-71) and cultured in RPMI 1640 medium (Gibco), supplemented with 10% heat-inactivated FBS (Corining) at standard culture conditions.

Nonviral in vitro Transfection: Nonviral cell transfection of adult-MDFs was performed using a Neon transfection system (Thermo Fisher Scientific). Once the cells (passage <P4) reached >80% confluency, they were detached and resuspended at a final concentration of 1.0×10^6 cells in 100 μL of electrolytic buffer. Cells were cotransfected with plasmids encoding for IL-4+SPA, and IL-10+SPA in a proportion of 1:1 (at 0.05 μg μL^{-1}). pCMV6-GFP (sham/empty vector) was used as a control at a concentration of 0.1 μg μL^{-1}. Following the procedure described by the manufacturer, cells were transfected for 30 ms with 1 pulse at 1425 V. This electric field allows for delivery of the molecular cargo into the cells via transient poration of the cell membrane and by driving the genetic material via electrophoresis. After transfection, cells were seeded in 6 wells plates and maintained in fibroblast basal medium with all the growth factor supplements provided by the vendor and supplemented with 10% exosome-depleted FBS (GIBCO, A27208-01). Successful transfection of the molecular cargo into the donor cells was verified via immunofluorescence microscopy (GFP-tag signal) and gene expression of each factor (mRNA) by quantitative reverse transcription polymerase chain reaction (qRT-PCR).

EV Isolation and Characterization: eEVs were isolated from culture media 24 h after transfection of the donor cells, as previously reported.[43,46,47] The culture media was centrifuged at 2000g for 30 min at 4 °C to remove dead cells and debris. After centrifugation, Total exosome isolation reagent (Thermo Fisher Scientific, 44-783-59) was added to the supernatant containing the cell-free culture media following manufacturer instructions. Pellets of eEVs were used fresh or stored at −80 °C for subsequent analysis. All eEVs were characterized in solution by measuring their concentration and size distribution via nanoparticle tracking analysis (NTA) and qRT-PCR was used to verify packing of the molecular cargo inside the eEVs prior to any experiment.

EV Isolation and Characterization—Cryo-Electron Microscopy (EM): The intact morphology of the eEVs was evaluated via Cryo-EM. To prepare the Cryo-EM grids, a small aliquot (3 μL) of the sample was applied to a Lacey carbon grid or a Lacey carbon grid with a continuous ultrathin carbon layer. After blotting away excess liquid, the grid was immediately plunged into liquid ethane to rapidly form a thin film of amorphous ice using the Vitrobot Mark IV system (Thermo Fisher Scientific, Hillsboro). The Vitrobot was operated at 4 °C and 100% humidity. The blotting force was set at +1. The blotting time was 3–5 s and the frozen grids were clipped into AutoGrids and transferred into Glacios CryoTEM (Thermo Fisher Scientific, Hillsboro. OR, USA), or stored in a liquid nitrogen tank. Cryo-EM images were captured with Falcon 3EC direct electron detector under linear mode on Glacios Cryo-EM. The microscope was operated at an acceleration voltage of 200 kV, and images were collected by using EPU software at 57 000× or 6700× nominal magnification.

EV Isolation and Characterization—Western Blot: eEV pellets were resuspended in 20 μL of Lysis buffer containing RIPA buffer (Thermo Fisher Scientific, 89900), phosphatase inhibitor cocktail (Sigma-Aldric, P5726-1), protease inhibitor cocktail (Roche, 4693116001), and 1×10^{-3} M phenyl-methylsulfonyl fluoride (PMSF, Thermo Scientific, 36 978), vortexed for 15 min at 4 °C and incubated overnight at −20 °C. The samples were once again vortexed for 15 min at 4 °C and centrifuged at 10 000 rpm

2210579 (15 of 20)

**ADVANCED
SCIENCE NEWS**

www.advancedsciencenews.com

**ADVANCED
MATERIALS**

www.advmat.de

for 30 min at 4 °C, and the cytosolic protein content was recovered and quantified via Bradford assay (Bio-Rad, 500006). 14 ug of total protein was combined with NuPAGE LDS Sample Buffer (4×) and NuPAGE Sample Reducing Agent (10×) (Thermo Fisher Scientific, NP007, NP009 respectively), heated 2 min at 85 °C and loaded into 10–20% Tris-Glycine mini gels (Thermo Fisher Scientific, XP10202BOX). Proteins were electrophoretically transferred to a nitrocellulose or Polyvinylidene difluoride (PVDF) membrane (Thermo Fisher Scientific, LC2001/LC2002). The membranes were washed with TBS-T 1× (Tris-Glycine transfer buffer and tween, Novex, and Thermo Fisher Scientific, respectively) and blocked with 5% BSA for 1 h at room temperature (RT). All antibodies were diluted in TBS-T and 2.5% BSA and incubated overnight at 4 °C (primary antibodies), or 1 h at RT (secondary antibodies). Finally, membranes were visualized using a C-DiGit LI-COR blot scanner. Table S2 (Supporting Information) contains the list of all antibodies used for this study.

Gene Expression Analyses: For this type of analysis, donor cells, monocytes, and eEVs were collected using TRizol reagent (Thermo Fisher Scientific, 15596018) to subsequently extract total RNA. Nanodrop 2000c Spectrophotometer (Thermo Fisher Scientific) was used to measure RNA concentrations and quality. Reverse transcription reactions were performed with the superscript VILO cDNA synthesis kit (Thermo Fisher Scientific, 11754050) using 80–2500 ng RNA in a 20 µL reaction, preserving equal amounts of cDNA throughout the samples. Taking the cDNA as a template, the mRNA expression levels were verified by qRT-PCR in donor cells and eEV, using predesigned primers (all the primers used in this study are listed in Table S3 of the Supporting Information). qRT-PCR reactions were performed using the QuantStudio 3 Real-Time PCR System with TaqMan fast advance Master Mix (Thermo Fisher Scientific, 4444964). Gene expression was normalized using the housekeeping gene GAPDH and all data presented as fold change relative to sham/control.

After bronchoalveolar lavage fluid (BALF) collection, the left lungs were preserved for protein isolation. To this end, lung samples were processed in Lysis buffer (as described in the Western Blot Section above) using a gentleMACS Dissociator (Miltenyi Biotec), with gentleMACS M tubes (Miltenyi Biotec, 130-093-236), subsequently centrifuged at max speed 15 min at 4 °C and stored for subsequent analysis.

In Vitro Assays Using Lipopolysaccharide (LPS): Monocytes RAW 264.7 were seeded overnight in 12-well culture plates at a density of 2.0×10^5 cells cm^{-2}. All the experiments described below were run using a minimum of 3 biological replicates and 3 technical replicates. Monocytes were challenged in vitro with Lipopolysaccharide (LPS, L4524, Sigma Aldrich) resuspended in RPMI 1640 plain medium at 2 different concentrations (100–1000 ng mL^{-1}). Non-treated cells were used as control. 24 h after LPS challenge, culture plates were imaged using brightfield under a Nikon Ti-2e microscope at 20× to evaluate cell morphology. Additionally, culture media was collected and stored at −80 °C for further analysis (e.g., protein analysis). Cells were collected using TRizol reagent, followed by RNA extraction and cDNA synthesis. The inflammatory response was evaluated by the expression of proinflammatory mediators (e.g., IL-6, IL-1β, iNOS, TNF-α, and KC) via qRT-PCR as already described. To test the dynamics of secretion of key proinflammatory mediators, monocytes RAW 264.7 cells were seeded overnight and treated with 100 ng mL^{-1} of LPS for 3–48 h. Dose-response experiments were conducted using three different doses of eEVs, including a high dose of 4×10^9 eEVs, a medium dose of 4×10^8 eEVs, and a low dose of 4×10^7 eEVs. eEVs were delivered to macrophages challenged with 100 ng mL^{-1} LPS (i.e., cotreatment) for 3 h (Figure S5A, Supporting Information). The inflammatory response based on the protein expression levels of proinflammatory cytokines IL-6, IL-1β, and TNF-α was characterized via U-Plex assay (K15069M-1, Meso Scale Diagnostics LLC) by electrochemiluminesmecence using the MESO QuickPlex SQ 120 instrument (Meso Scale Discovery platform) following manufacturer's instructions. Analysis was performed using the DISCOVERY WORKBENCH 4.0 Analysis Software.

Morphological Analysis: Cell morphology was analyzed using images captured after co- or post-treatment with eEVs. All images were analyzed using the ImageJ-FIJI software, where each cell was categorized and counted as either a nonactivated (i.e., circular shape) or an activated monocyte (i.e., spindle shape). A minimum of 3 images per biological and technical replicate were analyzed per condition and the data was presented as the percentage of activated cells based on the total number of counted cells.

Animal Husbandry: All experiments using mice were performed following procedures previously approved by the Animal Care and Use Committee at The Ohio State University (IACUC # 2016A00000074-R1). 8-15-week-old male BALB/c- (000651 strain) and C57BL/6 mice were purchased from Jackson Laboratory. Mice were acclimated for 1 week after arrival. Isoflurane inhalation was used to anesthetize all animals before all experimental procedures.

Biodistribution Analysis: For the biodistribution experiments, eEVs were labeled with a far-red-fluorescent cell membrane labeling kit (MIDCLARET-1KT, Sigma Aldrich), according to manufacturer instructions. For this experiment, all mice were grouped and selected randomly. 9-15-week-old male C57BL/6 were anesthetized with inhalation of 5% isoflurane and maintained with 2% while conducting the procedure (based on body weight). For this experiment fluorescently labeled eEVs were intranasally administered to mice. Briefly, mice were positioned on an endotracheal intubation stand (Kent Scientific) to allow delivery of the eEV dose. A 25 µL bolus of 1.61×10^{11} eEVs mL^{-1} (*IL-10+SPA* or sham loaded eEVs) fluorescently labeled and resuspended in saline solution was delivered through the left nostril of the mouse monitoring the respiration rate during the entire procedure to reduce discomfort. Control mice were subjected to delivery of a 25 µL bolus of saline solution. Mice were euthanized 12 h after eEV intranasal delivery, and major organs (i.e., brain, heart, lungs, liver, kidneys, pancreas, and spleen) were collected in 4% FBS (GIBCO) in phosphate buffer solution (PBS, Thermo Fisher Scientific) and stored at 4 °C for further characterization. To quantify eEV accumulation, all organs were imaged by using an in vivo imaging system (IVIS) Lumina II (PerkinElmer Inc) right after collection. Images were captured using stage A with an excitation-emission of 640 nm (Cy5.5) and 1s exposure time. All images were analyzed via comparative analysis of the fluorescent radiant efficiency units, and eEV accumulation in each organ was normalized using animals nontreated with eEVs (i.e., control group). Once imaged all major organs (i.e., heart, liver, kidneys, and spleen) were collected and cryopreserved in OCT for further characterization.

Immunohistochemistry: After performing the targeting experiment and imaging the organs with IVIS, lung tissue was embedded in optimal cutting temperature (OCT, Thermo Fisher Scientific) solution and frozen at −80 °C for subsequent analysis. All samples were cryosectioned at 10 µm thickness using a CryoStar NX50 cryostat (Thermo Fisher Scientific), and mounted on charged microscope slides (Thermo Fisher Scientific). Tissue samples were fixed with cold Acetone, permeabilized with a solution of 0.05% PBS Tween 20 buffer (PBS-T, Thermo Fisher Scientific), and stained with a DAPI (4′,6-diamidino-2-phenylindole, dihydrochloride) solution in PBS (1:10 000) for 2 min to visualize the nuclei of the cells. Samples were mounted using Vectashield Vibrance Antifade mounting medium (Vector Laboratories) and imaged using an inverted fluorescence microscope (Nikon Ti-2e). All immunohistochemistry images were captured at 60×. Finally, mean fluorescence intensity quantification for Far-Red signal (for labeled eEVs) was performed using ImageJ-FIJI software and normalized by the area of the region of interest.

Immunohistochemistry—DAB Staining: Right lung samples were fixed with prechilled acetone for 3 min at RT. After incubation, samples were immersed in methanol containing 10% H_2O_2 for 15 min at RT to inactivate endogenous peroxidases. Then, the samples were rinsed with 0.1% Triton-X in PBS-1X for 15 min. The slides were blocked with 10% NGS and aviding in PBS-1X solution for 30 min at RT. Then primary antibodies (Table S3, Supporting Information) were prepared in a solution containing 2.5% NGS with biotin in PBS-1X, and were incubated overnight at 4 °C. After primary incubation, the samples were rinsed with 0.1% Triton-X in PBS-1X. All samples were subsequently incubated for 1 hour with a biotinylated secondary antibody (Table S3, Supporting Information) in a solution containing 2.5% NGS. After incubation, the samples were rinsed and incubated using an ABC (avidin–biotin complex) (Vector laboratories) kit for 20 min. The samples were rinsed and a 3,3′-diaminobenzidine (DAB) solution was added to each sample. When the sections turned brown the reaction was stopped with ddH$_2$O. Then, hematoxylin stain (Vector lab-

**ADVANCED
SCIENCE NEWS**

www.advancedsciencenews.com

**ADVANCED
MATERIALS**

www.advmat.de

oratories) was added to each tissue sample for 5 min, and the samples were washed with ddH$_2$O. Finally, the samples were dehydrated using an alcohol gradient and then rinsed with xylene before mounting. IL-10 expression in the lung tissue was measured using ImageJ-FIJI software as the percentage of positive area and normalized by the total number of nuclei per section.[121]

In Vivo Evaluation of the eEVs Therapeutic Effect: For these experiments, 9–10-week-old male BALB/c mice were selected randomly and grouped into 5 experimental groups (with a minimum of 4 mice per condition), including a positive (i.e., LPS-challenged mice) and negative (i.e., animals treated with saline solution) control groups, and LPS-challenged mice treated with IL-4+SPA eEVs, IL-10+SPA eEVs, or sham eEVs. Animals were anesthetized with inhalation of 5% isoflurane and maintained with 2% while conducting the procedure (based on body weight). Mice were positioned on an endotracheal intubation stand (Kent Scientific) for intranasal delivery (through the left nostril) of a 25 µL bolus of 0.4 mg kg^{-1} of LPS resuspended in saline solution. Negative control mice received a 25 µL bolus of saline solution. The respiratory rate of the animals was monitored during the entire procedure to reduce discomfort. 6 h after LPS challenge, mice treated with eEVs were administered a 25 µL bolus of 5.82×10^{10} EVs mL^{-1} of *IL-10+SPA* eEVS, *IL-4+SPA* eEVs or sham eEVs resuspended in saline solution. For lung functional assessments, mice were anesthetized 12 h after being challenged with LPS, and tracheostomies were initiated with an 18G cannula. Mice were subjected to mechanical ventilation with a FlexiVent FX2 system (SCIREQ Inc) at 150 breathes min^{-1}, tidal volume of 10 mL kg^{-1}, and a positive end-expiratory pressure (PEEP) of 3 cm H2O prior to baseline measurements. To eliminate breathing efforts and measurement errors, pancuronium bromide (1 mg kg^{-1}, Sigma Aldrich) was administered intraperitoneally. Using a "Snapshot-150 perturbation," respiratory stiffness (Ers) and compliance (Crs) were measured from the forced oscillation technique (FOT) fitted to a single compartment model. Additionally, a broadband FOT maneuver ("Quick Prime-3 perturbation") was completed to capture the alveolar tissue stiffness/elastance (H). The negative pressure forced expiration (NPFE) extension of the FlexiVent then recorded forced expiratory volume by inflating the lungs to a pressure of +30 cmH2O over 1.2 seconds and then rapidly decreased to a negative pressure of 55 cmH2O. The forced expiratory volume was calculated from the flow-volume loop over 0.1 s (FEV0.1). Mice were euthanized, and lungs were inflated with 10% formalin, collected, and preserved for subsequent histological analysis.

Hematoxylin and Eosin (H&E) Staining and Morphometrical Analysis: Lung tissue was fixed in 10% formalin for 72 h, and subsequently, paraffin-embedded and sectioned for histologic analysis. Lung sections (n = 4 per animal) were stained with H&E to evaluate changes in tissue morphology. For morphometrical analysis, 4 lung fields captured at 90× magnification were randomly selected per section. For each field, a grid with 487.34 µm^2 (area per point) was used to count the number of alveolar units represented as alveoli per hpf (high power field), and the mean septal thickness. Moreover, the mean linear intercept was calculated as the inverse of the number of air-tissue interfaces to the next measured in microns as previously reported.[122,123]

Characterization of Bronchoalveolar Lavage Fluid (BALF): To collect the bronchoalveolar lavage fluid (BALF), the trachea of the mouse was exposed, and a tracheotomy was performed to introduce a 25G gauge needle. A 1 mL syringe with 800 µL of cold sterile PBS was used to gently wash the lungs twice through the trachea. Once collected, BALF samples (600–700 µL) were centrifuged at 400g for 10 min at 4 °C, and stored for downstream analysis. BALF samples were subjected to total protein quantification via Bradford assay compared to a BSA standard curve. For BALF differential cell counts, the pellet containing all free-floating cells from the lung was resuspended in Red Blood Cell Lysis Solution (Miltenyi Biotec), to induce selective lysis of the erythrocytes, following the manufacturer's protocol. Cell suspensions were subsequently cytocentrifuged onto Epredia Cytoslide microscope slides (Thermo Fisher Scientific) using a Cytospin at 300g for 3 min. The slides were then air-dried and stained using the Hemacolor Stain Set (Sigma Aldrich, 65044-93) and imaged using a color camera on a Nikon Ti-2e microscope. All images were captured at 40× and analyzed using ImageJ-FIJI software, where the different cell populations present in the BALF samples (e.g., macrophages, neutrophils, lymphocytes) were identified and counted. A minimum of 5 pictures were analyzed per sample.

Enzyme-Linked Immunosorbent Assay: Protein expression levels for proinflammatory factors including interleukin 6 (IL-6), interleukin-1 beta (IL-1β), and tumor necrosis factor alpha (TNF-α) were quantified via ELISA, using the commercially available kits DY406, DY401, and DY410 (R&D Systems), respectively. IL-4 and IL-10 protein content associated with the eEVs was evaluated using the commercially available ELISA kits DY404 and DY417 (R&D Systems), respectively. For these assays, protein isolation was performed as previously described. In order to detect the presence of SPA as a ligand on the surface of the eEV, a commercial mouse SPA ELISA kit (Novus Biologicals, NBP2-76693) was used following the protocol described by the manufacturer using intact *IL-4+SPA, IL-10+SPA*, or sham eEVs.

Untargeted Metabolomics Analysis of BALF: Metabolites from BALF samples were extracted by adding 400 µL of ice-cold methanol:chloroform LC/MS grade (Optima, Fisher Chemical) (9:1) to 100 mL of clarified BALF, resuspended thoroughly and filtered using 0.2 µm nylon syringe filters (Thermo Scientific). All samples were normalized by volume to enable relative quantitative comparison between samples. The extracted metabolites were dried on a sample concentrator (Eppendorf® Vacufuge) at 45 °C for 1 h. The dried samples were reconstituted in 50 µL of LC/MS grade water (Optima, Fisher Chemical) with 0.1% formic acid LC/MS grade (Optima, Fisher Chemical) and 5% methanol (Optima, Fisher Chemical). Samples were mixed by vortexing, sonicated for 15 min, centrifuged at 14 000g for 1 min, and transferred to liquid chromatography low-volume vials (Waters) for liquid chromatography–tandem mass spectrometry (LC–MS/MS) analysis. The same extraction procedure was performed with PBS (sample blank) and a pooled QC sample was prepared by mixing 2.5 mL of each sample in a single vial. An additional vial sample was prepared as the extraction control, containing the solution used for resuspension of each sample (water with 5% methanol and 0.1% formic acid). No internal standard was used in this experiment. Differences in metabolite abundances in each experimental group were estimated based on relative comparisons between equally treated samples. At least 3 biological replicates were run for each condition.

The untargeted LC–MS/MS analysis was performed on a 6545 Q-TOF LC/MS coupled to a high-performance liquid chromatography (HPLC) system (Agilent 1290 Infinity LC). In each run, 3 mL of sample were injected into the HPLC system for separation, using a SB-C18 column (2.1×100 mm, 2.7 mm particle size, 120 Å pore size, InfinityLab Poroshell 120). The column was maintained at 40 °C during the run, using a flow rate of 0.2 mL min^{-1}, water with 0.1% formic acid as solvent A and methanol with 0.1% formic acid as solvent B. The gradient used for the chromatographic run started at 2% B for 15 min, followed by 90% B for 1 min, then 98% B for 1 min, and back to 2% B for 1 min. After each run, the column was equilibrated at 2% B for 8 min. The MS system was calibrated using a standard Agilent ESI Low Concentration tune solution. System stability was checked by analyzing pooled QC regularly in between batches of the run. All samples were analyzed in positive and negative modes using data-dependent acquisition mode. MS spectra (m/z 50–1700. Scan rate 5 spectra s^{-1}) were followed by data-dependent MS/MS spectra (m/z 50–1700. Scan 10 spectra s^{-1}) for the 5 most intense ions per scan with a dynamic exclusion of 30 s. Ion selection was based on an intensity threshold of 3000, fragmented using a collision energy ramp (CE 10–80 eV). The injection of samples was randomized, and each sample was analyzed three times, including the extraction control, sample blank, and pooled QC samples.

Data processing and analysis included the conversion of raw .d files to .mzXML using MSconvert (ProteoWizard).[124] Feature detection was carried out in MZmine v.2.53[125] using the settings listed in Table S4. Statistical analyses were performed using Metaboanalyst 5.0.[126] Three complementary approaches were integrated for feature annotation: 1) accurate m/z search, based on compounds from the Human Metabolome Database (HMDB); 2) spectral search, matching MS/MS fragmentation patterns with mass spectral records from MassBank of North America (MoNA); and 3) de novo molecular structure identification, using

**ADVANCED
SCIENCE NEWS**

www.advancedsciencenews.com

**ADVANCED
MATERIALS**

www.advmat.de

SIRIUS (5.5.7) for structure prediction based on MS and MS/MS isotope and fragmentation patterns analysis. KEGG IDs of identified compounds were assigned when possible and pathway analysis was performed in Metascape.[127] The metabolomics datasets were deposited in Massive (https://massive.ucsd.edu/) with the identifiers MSV000089900 for the positive mode data files, and MSV000089807 for the negative mode data files.

Statistical Analysis: All data were tested for normality using Shapiro–Wilk test, and outliers were tested using ROUT method with $Q = 1\%$. Data that followed a normal distribution were analyzed using one-way analysis of variance (ANOVA) with post hoc least significant difference test (Fisher LSD method) or two-tailed *t*-test as pertinent. Data that were not normally distributed were analyzed using nonparametric statistical analysis, i.e., ANOVA on ranks with post hoc Tukey test. All data were graphed as mean ± standard error of the mean (S.E.M.). For in vivo experiments $n = 4$ biological replicates were used and $n = 3$–4 for in vitro experiments. The statistical significance level was defined as $P < 0.05$ for hypothesis testing. The analyses were run using the statistical software Sigma Plot 14 and GraphPad Prism 9.

Supporting Information

Supporting Information is available from the Wiley Online Library or from the author.

Conflict of Interest

The authors declare no conflict of interest.

Data Availability Statement

The data that support the findings of this study are available from the corresponding author upon reasonable request. The metabolomics datasets are deposited in Massive (http://massive.uscd.edu) with the identifiers MSV000089900 and MSV000089807 for the positive and negative mode data files, respectively.

[1] M. Moss, B. T. Thompson, in *Acute Respiratory Distress Syndrome*, 2nd Ed. (Ed: A. M. K. Choi), Informa Healthcare USA, Inc, New York, **2010**, pp. 1–45.

[2] G. D. Rubenfeld, M. S. Herridge, *Chest* **2007**, *131*, 554.

[3] E. R. Johnson, M. A. Matthay, *J. Aerosol. Med. Pulm. Drug Delivery* **2010**, *23*, 243.

[4] J. Maca, O. Jor, M. Holub, P. Sklienka, F. Bursa, V. Janout, P. Sevcik, *Respir. Care.* **2017**, *62*, 113.

[5] S. Kaku, C. D. Nguyen, N. N. Htet, D. Tutera, J. Barr, H. S. Paintal, W. G. Kuschner, *J. Intensive Care Med.* **2020**, *35*, 723.

[6] L. A. Huppert, M. A. Matthay, L. B. Ware, *Semin. Respir. Crit. Care Med.* **2019**, *40*, 31.

[7] M. A. Matthay, R. L. Zemans, *Annu. Rev. Pathol.* **2011**, *6*, 147.

[8] S. Han, R. K. Mallampalli, *J. Immunol.* **2015**, *194*, 855.

[9] M. Ragaller, T. Richter, *J. Emerg. Trauma Shock.* **2010**, *3*, 43.

[10] M. Bhatia, S. Moochhala, *J. Pathol. Clin. Res.* **2004**, *202*, 145.

[11] S. Rajasekaran, D. Pattarayan, P. Rajaguru, P. S. Sudhakar Gandhi, R. K. Thimmulappa, *J. Cell. Physiol.* **2016**, *231*, 2097.

[12] Y. Huang, M. Crawford, N. Higuita-Castro, P. Nana-Sinkam, S. N. Ghadiali, *FASEB J.* **2012**, *26*, 3351.

[13] M. A. Matthay, L. B. Ware, G. A. Zimmerman, *J. Clin. Invest.* **2012**, *122*, 2731.

[14] B. T. Thompson, R. C. Chambers, K. D. Liu, *N. Engl. J. Med.* **2017**, *377*, 562.

[15] F. F. Cruz, D. J. Weiss, P. R. Rocco, *Expert Opin. Biol. Ther.* **2016**, *16*, 1353.

[16] W. Xu, N.-N. Sun, H.-N. Gao, Z.-Y. Chen, Y. Yang, B. Ju, L.-L. Tang, *Sci. Rep.* **2021**, *11*, 2933.

[17] P. G. Gibson, L. Qin, S. H. Puah, *Med. J. Aust.* **2020**, *213*, 54.e51.

[18] D. Tang, P. Comish, R. Kang, *PLoS Pathog.* **2020**, *16*, e1008536.

[19] B. Gosangi, A. N. Rubinowitz, D. Irugu, C. Gange, A. Bader, I. Cortopassi, *Emerg. Radiol.* **2022**, *29*, 23.

[20] J. Han, Y. Li, Y. Li, *Stem Cells Int.* **2019**, *2019*, 5432134.

[21] R. Guillamat-Prats, M. Camprubí-Rimblas, J. Bringué, N. Tantinyà, A. Artigas, *Ann. Transl. Med.* **2017**, *5*, 446.

[22] B. Xu, S.-s. Chen, M.-z. Liu, C.-x. Gan, J.-q. Li, G.-h. Guo, *Life Sci.* **2020**, *254*, 117766.

[23] T. Maron-Gutierrez, J. G. Laffey, P. Pelosi, P. R. M. Rocco, *Curr. Opin. Crit. Care* **2014**, *20*, 122.

[24] M. Krause, T. G. Phan, H. Ma, C. G. Sobey, R. Lim, *Front. Neurol.* **2019**, *10*, 656.

[25] A. S. Lee, C. Tang, M. S. Rao, I. L. Weissman, J. C. Wu, *Nat. Med.* **2013**, *19*, 998.

[26] S. Rajasekaran, D. Pattarayan, P. Rajaguru, P. S. Sudhakar Gandhi, R. K. Thimmulappa, *J. Cell. Physiol.* **2016**, *231*, 2097.

[27] F. Benz, S. Roy, C. Trautwein, C. Roderburg, T. Luedde, *Int. J. Mol. Sci.* **2016**, *17*, 78.

[28] M. S. Al-Dosari, X. Gao, *AAPS J.* **2009**, *11*, 671.

[29] C. L. Hisey, A. Artuyants, G. Guo, V. Chang, G. Reshef, M. Middleditch, B. Jacob, L. W. Chamley, C. Blenkiron, *J. Extracell. Biol.* **2022**, *1*, e60.

[30] T. N. Lamichhane, S. Sokic, J. S. Schardt, R. S. Raiker, J. W. Lin, S. M. Jay, *Tissue Eng., Part B* **2015**, *21*, 45.

[31] W. Stoorvogel, M. J. Kleijmeer, H. J. Geuze, G. Raposo, *Traffic* **2002**, *3*, 321.

[32] R. Kalluri, V. S. LeBleu, *Science* **2020**, *367*, eaau6977.

[33] Z. H. Kwok, K. Ni, Y. Jin, *Cells* **2021**, *10*, 965.

[34] K. O'Brien, K. Breyne, S. Ughetto, L. C. Laurent, X. O. Breakefield, *Nat. Rev. Mol. Cell Biol.* **2020**, *21*, 585.

[35] D. Ha, N. Yang, V. Nadithe, *Acta Pharm. Sin. B* **2016**, *6*, 287.

[36] R. Kalluri, V. S. LeBleu, *Science* **2020**, *367*, eaau6977.

[37] K. Khalaj, R. L. Figueira, L. Antounians, G. Lauriti, A. Zani, *J. Extracell. Vesicles* **2020**, *9*, 1795365.

[38] M. J. McVey, M. Maishan, K. E. C. Blokland, N. Bartlett, W. M. Kuebler, *Am. J. Physiol.: Lung Cell. Mol. Physiol.* **2019**, *316*, L977.

[39] E. N. Worthington, J. S. Hagood, *Int. J. Mol. Sci.* **2020**, *21*, 2318.

[40] E. I. Buzas, *Nat. Rev. Immunol.* **2023**, *23*, 236.

[41] B. Gantenbein, S. Tang, J. Guerrero, N. Higuita-Castro, A. I. Salazar-Puerta, A. S. Croft, A. Gazdhar, D. Purmessur, *Front. Bioeng. Biotechnol.* **2020**, *8*, 59846.

[42] K. W. Witwer, J. Wolfram, *Nat. Rev. Mater.* **2021**, *6*, 103.

[43] L. Ortega-Pineda, A. Sunyecz, A. I. Salazar-Puerta, M. A. Rincon-Benavides, D. Alzate-Correa, A. L. Anaparthi, E. Guilfoyle, L. Mezache, H. L. Struckman, S. Duarte-Sanmiguel, B. Deng, D. W. McComb, D. J. Dodd, W. R. Lawrence, J. Moore, J. Zhang, E. Reategui, R. Veeraraghavan, M. T. Nelson, D. Gallego-Perez, N. Higuita-Castro, *Adv. Healthcare Mater.* **2022**, *11*, 2100805.

[44] S. Duarte-Sanmiguel, A. Panic, D. J. Dodd, A. Salazar-Puerta, J. T. Moore, W. R. Lawrence, K. Nairon, C. Francis, N. Zachariah, W. Mccoy, R. Turaga, A. Skardal, W. E. Carson, N. Higuita-Castro, D. Gallego-Perez, *Adv. Healthcare Mater.* **2021**, *11*, 2101619.

[45] S. Duarte-Sanmiguel, N. Higuita-Castro, D. Gallego-Perez, *Methods Mol. Biol.* **2020**, *2050*, 79.

[46] S. Tang, A. Salazar-Puerta, J. Richards, S. Khan, J. A. Hoyland, D. Gallego-Perez, B. Walter, N. Higuita-Castro, D. Purmessur, *Eur. Cell Mater.* **2021**, *41*, 90.

[47] L. R. Lemmerman, M. H. H. Balch, J. T. Moore, D. Alzate-Correa, M. A. Rincon-Benavides, A. Salazar-Puerta, S. Gnyawali, H. N. Harris, W. Lawrence, L. Ortega-Pineda, L. Wilch, I. B. Risser, A. J. Maxwell, S. Duarte-Sanmiguel, D. Dodd, G. P. Guio-Vega, D. M. Mctigue, W. D. Arnold, S. M. Nimjee, C. K. Sen, S. Khanna, C. Rink, N. Higuita-Castro, D. Gallego-Perez, *Sci. Adv.* **2021**, *7*, eabd4735.

[48] D. Gallego-Perez, D. Pal, S. Ghatak, V. Malkoc, N. Higuita-Castro, S. Gnyawali, L. Chang, W.-C. Liao, J. Shi, M. Sinha, K. Singh, E. Steen, A. Sunyecz, R. Stewart, J. Moore, T. Ziebro, R. G. Northcutt, M. Homsy, P. Bertani, W. Lu, S. Roy, S. Khanna, C. Rink, V. B. Sundaresan, J. J. Otero, L. J. Lee, C. K. Sen, *Nat. Nanotechnol.* **2017**, *12*, 974.

[49] M. A. Rincon-Benavides, N. C. Mendonca, T. Z. Cuellar-Gaviria, A. I. Salazar-Puerta, L. Ortega-Pineda, B. N. Blackstone, B. Deng, D. W. Mccomb, D. Gallego-Perez, H. M. Powell, N. Higuita-Castro, *Adv. Ther.* **2023**, *6*, 2200197.

[50] M. Sarker, D. Jackman, V. Booth, *Biochemistry* **2011**, *50*, 4867.

[51] S. D. King, S. Y. Chen, *Am. J. Physiol. Cell Physiol.* **2020**, *319*, C316.

[52] N. Nathan, J. Taytard, P. Duquesnoy, G. Thouvenin, H. Corvol, S. Amselem, A. Clement, *Int. J. Biochem. Cell Biol.* **2016**, *81*, 151.

[53] R. J. Schutte, A. Parisi-Amon, W. M Reichert, *J. Biomed. Mater. Res. A* **2009**, *88*, 128.

[54] R. Z. Murray, J. L. Stow, *Front. Immunol.* **2014**, *5*, 538.

[55] L. Zhang, S. Tan, Y. Liu, H. Xie, J. Wang, *Biomater. Appl.* **2019**, *33*, 935.

[56] S. R. Bates, A. S. Kazi, J.-Q. Tao, K. J. Yu, D. S. Gonder, S. I. Feinstein, A. B. Fisher, *Am. J. Physiol Lung. Cell Mol. Physiol.* **2008**, *295*, L658.

[57] V. Agrawal, K. Smart, T. Jilling, E. Hirsch, *PLoS One* **2013**, *8*, e63990.

[58] Z. Lanyu, H. Feilong, *Biomed. Pharmacother.* **2019**, *113*, 108748.

[59] A. Mohan, S. Agarwal, M. Clauss, N. S. Britt, N. K. Dhillon, *Respir. Res.* **2020**, *21*, 175.

[60] D. R. Potter, B. Y. Gibb, X. Deng, P. P. Togaratti, R. H. Croze, A. Srivastava, A. Trivedi, M. Matthay, J. B. Holcomb, M. A. Schreiber, S. Pati, *Trauma Acute Care Surgery* **2018**, *84*, 245.

[61] D. E. Murphy, O. G. De Jong, M. Brouwer, M. J. Wood, G. Lavieu, R. M. Schiffelers, P. Vader, *Exp. Mol. Med.* **2019**, *51*, 32.

[62] N. Morimoto, T. Ito, S. Takemoto, M. Katakami, N. Kanda, H. Tada, S. Tanaka, S. Teramukai, K. Kawai, Y. Nakamura, Y. Kasai, Y. Masayuki, T. Maekawa, A. Shimizu, S. Suzuki, *Int. Wound J.* **2014**, *11*, 183.

[63] R. L. Thangapazham, T. N. Darling, J. Meyerle, *Int. J. Mol. Sci.* **2014**, *15*, 8407.

[64] Á. Sierra-Sánchez, K. H. Kim, G. Blasco-Morente, S. Arias-Santiago, *npj Regener. Med.* **2021**, *6*, 35.

[65] S.-K. Han, in *Innovations and Advances in Wound Healing*, (Ed: S.-K. Han) Springer Nature, Singapore, **2023**, pp. 97–126.

[66] P. Lai, J. Weng, L. Guo, X. Chen, X. Du, *Nonai Roka Seigyo to Baiomaka: Kiban Kenkyu to Shokuhin Sozai* **2019**, *7*, 6.

[67] H. S. Hwang, H. Kim, G. Han, J. W. Lee, K. Kim, I. C. Kwon, Y. Yang, S. H. Kim, *Int. J. Mol. Sci.* **2021**, *22*, 5487.

[68] P. D. Robbins, A. Dorronsoro, C. N. Booker, *J. Clin. Invest.* **2016**, *126*, 1173.

[69] M. Burgelman, C. Vandendriessche, R. E. Vandenbroucke, *Pharmaceuticals* **2021**, *14*, 829.

[70] W. Fitzgerald, M. L. Freeman, M. L. Lederman, E. Vasilieva, R. Romero, L. A. Margoris, *Sci. Rep.* **2018**, *8*, 8973.

[71] V. Sueblinvong, D. J. Weiss, *Curr. Opin. Pharmacol.* **2009**, *9*, 268.

[72] P. Wang, P. Wu, M. I. Siegel, R. W. Egan, M. M. Billah, *J. Biol. Chem.* **1995**, *270*, 9558.

[73] C.-J. Lo, M. Fu, H. G. Cryer, *J. Surg. Res.* **1998**, *79*, 179.

[74] F. Huaux, T. Liu, B. McGarry, M. Ullenbruch, S. H. Phan, *J. Immunol.* **2003**, *170*, 2083.

[75] M. K. Levings, J. W. Schrader, *J. Immunol.* **1999**, *162*, 5224.

[76] P. H. Hart, G. F. Vitti, R. Burgess, G. A. Whitty, D. S. Piccoli, J. A. Hamilton, *Proc. Natl. Acad. Sci. USA* **1989**, *86*, 3803.

[77] J. Lötvall, A. F. Hill, F. Hochberg, E. I. Buzás, D. Di Vizio, C. Gardiner, Y. S. Gho, I. V. Kurochkin, S. Mathivanan, P. Quesenberry, S. Sahoo, H. Tahara, M. H. Wauben, K. W. Witwer, C. Théry, *J. Extracell Vesicles* **2014**, *3*, 26913.

[78] S. A. A. Kooijmans, R. M. Schiffelers, N. Zarovni, R. Vago, *Pharmacol. Res.* **2016**, *111*, 487.

[79] P. Lara, A. B. Chan, L. J. Cruz, A. F. G. Quest, M. J. Kogan, *Pharmaceutics* **2020**, *12*, 1022.

[80] H. Kim, D. Kim, H. Nam, S. Moon, Y. L. Kwon, J. B. Lee, *Methods* **2020**, *177*, 80.

[81] C. Liu, C. Su, *Theranostics* **2019**, *9*, 1015.

[82] B. de Jong, E. R. Barros, J. G. J. Hoenderop, J. P. Rigalli, *Pharmaceutics* **2020**, *12*, 1006.

[83] V. Castranova, J. Rabovsky, J. H. Tucker, P. R. Miles, *Toxicol. Appl. Pharmacol.* **1988**, *93*, 472.

[84] A. C. Stanley, P. Lacy, *Physiology* **2010**, *25*, 218.

[85] A. S. Farivar, S. M. Woolley, C. H. Fraga, K. Byrne, M. S. Mulligan, *Am. J. Transplant.* **2004**, *4*, 346.

[86] S. R. Bates, *Cell. Physiol. Biochem.* **2010**, *25*, 041.

[87] H. Domscheit, M. A. Hegeman, N. Carvalho, P. M. Spieth, *Front. Physiol.* **2020**, *11*, 36.

[88] I. Martin, K. Cabán-Hernández, O. Figueroa-Santiago, A. M. Espino, *J. Immunol.* **2015**, *194*, 3924.

[89] K. Fukunaga, P. Kohli, C. Bonnans, L. E. Fredenburgh, B. D. Levy, *J. Immunol.* **2005**, *174*, 5033.

[90] K. Modelska, J.-F. Pittet, H. G. Folkesson, V. C. Broaddus, M. A. Matthay, *Am. J. Respir. Crit. Care Med.* **1999**, *160*, 1450.

[91] L. Frank, J. R. Bucher, R. J. Roberts, *J. Appl. Physiol. Respir. Environ. Exerc. Physiol.* **1978**, *45*, 699.

[92] P. E. Parsons, M. D. Eisner, B. T. Thompson, M. A. Matthay, M. Ancukiewicz, G. R. Bernard, A. P. Wheeler, *Crit. Care Med.* **2005**, *33*, 1.

[93] M. A. Matthay, R. L. Zemans, G. A. Zimmerman, Y. M. Arabi, J. R. Beitler, A. Mercat, M. Herridge, A. G. Randolph, C. S. Calfee, *Nat. Rev. Dis. Primers* **2019**, *5*, 18.

[94] T. Sakuma, K. Takahashi, N. Ohya, O. Kajikawa, T. R. Martin, K. H. Albertine, M. A. Matthay, *Am. J. Physiol.* **1999**, *276*, L137.

[95] R. Fox-Dewhurst, M. K. Alberts, O. Kajikawa, E. Caldwell, M. C. Johnson, S. J. Skerrett, R. B. Goodman, J. T. Ruzinski, V. A. Wong, E. Y. Chi, T. R. Martin, *Am J. Respir. Crit. Care Med.* **1997**, *155*, 2030.

[96] J. H. Vernooy, M. A. Dentener, R. J. van Suylen, W. A. Buurman, E. F. Wouters, *Am. J. Respir. Cell Mol. Biol.* **2001**, *24*, 569.

[97] H. S. Kulkarni, J. S. Lee, J. A. Bastarache, W. M. D. Kuebler, G. P. Downey, G. M. Albaiceta, W. A. Altemeier, A. Artigas, J. H. T. Bates, C. S. Calfee, C. S. Dela Cruz, R. P. Dickson, J. A. Englert, J.

I. Everitt, M. B. Fessler, A. E. Gelman, K. W. Gowdy, S. D. Groshong, S. Herold, R. J. Homer, J. C. Horowitz, C. C. W. Hsia, K. Kurahashi, V. E. Laubach, M. R. Looney, R. Lucas, N. S. Malgarmurti, A. M. Manicone, T. R. Martin, S. Matalon, et al., *Am. J. Respir. Cell Mol. Biol.* **2022**, *66*, e1.

[98] F. Aeffner, B. Bolon, I. C. Davis, *Toxicol. Pathol.* **2015**, *43*, 1074.

[99] S. Stukas, R. L. Hoiland, J. Cooper, S. Thiara, D. E. Griesdale, A. D. Thomas, M. M. Orde, J. C. English, L. Y. C. Chen, D. Foster, A. R. Mitra, K. Romano, D. D. Sweet, J. J. Ronco, H. D. Kanji, Y. R. Chen, S. L. Wong, C. L. Wellington, M. S. Sekhon, *Crit. Care Explor.* **2020**, *2*, e0203.

[100] C. R. Evans, A. Karnovsky, M. A. Kovach, T. J. Standiford, C. F. Burant, K. A. Stringer, *J. Proteome Res.* **2014**, *13*, 640.

[101] M. A. Hidalgo, M. D. Carretta, R. A. Burgos, *Front. Physiol.* **2021**, *12*, 668330.

[102] S.-M. Kang, J. C. Park, M. J. Shin, H. Lee, J. Oh, D. H. Ryu, G. S. Hwang, J. H. Chung, *Clin. Biochem.* **2011**, *44*, 293.

[103] C. I. Cruickshank-Quinn, S. Mahaffey, M. J. Justice, G. Hughes, M. Armstrong, R. P. Bowler, R. Reisdorph, I. Petrache, N. Reisdorph, *PLoS One* **2014**, *9*, e101855.

[104] A. Lauer, M. Burkard, H. Niessner, C. Leischner, O. Renner, C. Vollbracht, H. Michels, C. Busch, T. Sinnberg, S. Venturelli, *Nutrients* **2021**, *13*, 2366.

[105] A. C. Carr, S. Maggini, *Nutrients* **2017**, *9*, 1211.

[106] B. J. Fisher, D. Kraskauskas, E. J. Martin, D. Farkas, J. A. Wegelin, D. Brophy, K. R. Ward, N. F. Voelkel, A. Alpha, I. Fowler, R. Natarajan, *Am. J. Physiol.: Lung Cell. Mol. Physiol.* **2012**, *303*, L20.

[107] A. Faulkner, A. Tamiato, W. Cathery, A. Rampin, C. M. Caravaggi, E. Jover, S. Allen, H. Mellor, D. Hauton, L. C. Heather, G. Spinetti, P. Madeddu, *Diabetologia* **2020**, *63*, 2205.

[108] S. Liu, J. Yang, Z. Wu, *Mediators Inflammation* **2021**, *2021*, 1.

[109] Y. Zhou, D. J. Schneider, M. R. Blackburn, *Pharmacol. Ther.* **2009**, *123*, 105.

[110] L. Liaudet, J. G. Mabley, P. Pacher, L. Virag, F. G. Soriano, A. Marton, G. Hasko, E. A. Deitch, C. Szabo, *Ann. Surg.* **2002**, *235*, 568.

[111] N. Wang, E. Li, H. Deng, L. Yue, L. Zhou, R. Su, B. He, C. Lai, G. Li, Y. Gao, W. Zhou, Y. Gao, *J. Pharm. Anal.* **2023**, *13*, 11.

[112] B. Mao, B. Guo, X. Tang, Q. Zhang, B. Yang, J. Zhao, S. Cui, H. Zhang, *Nutrients* **2022**, *14*, 2830.

[113] J. Xu, T. Pan, X. Qi, R. Tan, X. Wang, Z. Liu, Z. Tao, H. Qu, Y. Zhang, H. Chen, Y. Wang, J. Zhang, J. Wang, J. Liu, *Respir. Res.* **2020**, *21*, 99.

[114] O. M. E. Abdel-Salam, E. R. Youness, N. A. Mohammed, S. M. Y. Morsy, E. A. Omara, A. A. Sleem, *J. Med. Food.* **2014**, *17*, 588.

[115] K. M. Landolf, S. M. Lemieux, C. Rose, J. P. Johnston, C. D. Adams, J. Altshuler, K. Berger, D. Dixit, M. K. Effendi, M. S. Heavner, D. Lemieux, A. J. Littlefield, A. M. Nei, K. A. Owusu, M. Rinehart, B. Robbins, G. E. Rouse, M. L. Thompson Bastin, *Pharmacother.: J. Hum. Pharmacol. Drug Ther.* **2022**, *42*, 71.

[116] B. Abiri, M. Vafa, *Clin. Nutr. ESPEN* **2021**, *43*, 25.

[117] L. Zhang, B. Li, D. Zhang, Z. Wang, Y. Zhao, Q. Yu, *Physiol. Int.* **2022**, *109*, 215.

[118] M. Kaveh, N. Eftekhar, M. H. Boskabady, *Iran J. Basic. Med. Sci.* **2019**, *22*, 255.

[119] M. Sharifi-Rad, N. V. Anil Kumar, P. Zucca, E. M. Varoni, L. Dini, E. Panzarini, J. Rajkovic, P. V. Tsouh Fokou, E. Azzini, I. Peluso, A. Prakash Mishra, M. Nigam, Y. El Rayess, M. E. Beyrouthy, L. Polito, N. Martins, M. Martorell, A. O. Docea, W. N. Setzer, D. Calina, W. C. Cho, J. Sharifi-Rad, *Front. Physiol.* **2020**, *11*, 694.

[120] E. M. Pålsson-McDermott, L. A. J O'Neill, *Cell Res.* **2020**, *30*, 300.

[121] A. R. Crowe, W. Yue, *Bio. Protoc.* **2019**, *9*, e3465.

[122] Z. J. Pua, B. S. Stonestreet, A. Cullen, A. Shahsafaei, G. B. Sadowska, M. E. Sunday, *J. Histochem. Cytochem.* **2005**, *53*, 1469.

[123] S. T. Tsikis, S. C. Fligor, T. I. Hirsch, A. Pan, L. J. Yu, H. Kishikawa, M. M. Joiner, P. D. Mitchell, M. Puder, *Sci. Rep.* **2022**, *12*, 10245.

[124] M. C. Chambers, B. Maclean, R. Burke, D. Amodei, D. L. Ruderman, S. Neumann, L. Gatto, B. Fischer, B. Pratt, J. Egertson, K. Hoff, D. Kessner, N. Tasman, N. Shulman, B. Frewen, T. A. Baker, M.-Y. Brusniak, C. Paulse, D. Creasy, L. Flashner, K. Kani, C. Moulding, S. L. Seymour, L. M. Nuwaysir, B. Lefebvre, F. Kuhlmann, J. Roark, P. Rainer, S. Detlev, T. Hemenway, et al., *Nat. Biotechnol.* **2012**, *30*, 918.

[125] T. Pluskal, S. Castillo, A. Villar-Briones, M. M. Z. Orešič, *BMC Bioinformatics* **2010**, *11*, 395.

[126] Z. Pang, G. Zhou, J. Ewald, L. Chang, O. Hacariz, N. Basu, J. Xia, *Nat. Protoc.* **2022**, *17*, 1735.

[127] A. Karnovsky, T. Weymouth, T. Hull, V. G Tarcea, G. Scardoni, C. Laudanna, M. A. Sartor, K. A. Stringer, H. V. Jagadish, C. Burant, B. Athey, G. S. Omenn, *Bioinformatics* **2011**, *28*, 373.